Monthly Notices of the ROYAL ASTRONOMICAL SOCIETY

MNRAS **452,** 575–596 (2015) doi:10.1093/mnras/stv1340

The Illustris simulation: the evolving population of black holes across cosmic time

Debora Sijacki,[1★] Mark Vogelsberger,[2] Shy Genel,[3,4†] Volker Springel,[5,6] Paul Torrey,[2,3,7] Gregory F. Snyder,[8] Dylan Nelson[3] and Lars Hernquist[3]

[1]*Institute of Astronomy and Kavli Institute for Cosmology, University of Cambridge, Madingley Road, Cambridge CB3 0HA, UK*
[2]*Department of Physics, Kavli Institute for Astrophysics and Space Research, Massachusetts Institute of Technology, Cambridge, MA 02139, USA*
[3]*Harvard-Smithsonian Center for Astrophysics, 60 Garden Street, Cambridge, MA 02138, USA*
[4]*Department of Astronomy, Columbia University, 550 West 120th Street, New York, NY 10027, USA*
[5]*Heidelberg Institute for Theoretical Studies, Schloss-Wolfsbrunnenweg 35, D-69118 Heidelberg, Germany*
[6]*Zentrum für Astronomie der Universität Heidelberg, ARI, Mönchhofstr. 12-14, D-69120 Heidelberg, Germany*
[7]*Caltech, TAPIR, Mailcode 350-17, California Institute of Technology, Pasadena, CA 91125, USA*
[8]*Space Telescope Science Institute, 3700 San Martin Dr, Baltimore, MD 21218, USA*

Accepted 2015 June 12. Received 2015 June 12; in original form 2014 August 28

ABSTRACT

We study the properties of black holes and their host galaxies across cosmic time in the Illustris simulation. Illustris is a large-scale cosmological hydrodynamical simulation which resolves a (106.5 Mpc)^3 volume with more than 12 billion resolution elements and includes state-of-the-art physical models relevant for galaxy formation. We find that the black hole mass density for redshifts $z = 0$–5 and the black hole mass function at $z = 0$ predicted by Illustris are in very good agreement with the most recent observational constraints. We show that the bolometric and hard X-ray luminosity functions of active galactic nuclei (AGN) at $z = 0$ and 1 reproduce observational data very well over the full dynamic range probed. Unless the bolometric corrections are largely underestimated, this requires radiative efficiencies to be on average low, $\epsilon_{\rm r} \lesssim 0.1$, noting however that in our model radiative efficiencies are degenerate with black hole feedback efficiencies. Cosmic downsizing of the AGN population is in broad agreement with the findings from X-ray surveys, but we predict a larger number density of faint AGN at high redshifts than currently inferred. We also study black hole–host galaxy scaling relations as a function of galaxy morphology, colour and specific star formation rate. We find that black holes and galaxies co-evolve at the massive end, but for low mass, blue and star-forming galaxies there is no tight relation with either their central black hole masses or the nuclear AGN activity.

Key words: methods: numerical – galaxies: formation – quasars: supermassive black holes – cosmology: theory.

1 INTRODUCTION

Accretion on to supermassive black holes has been identified as the most likely mechanism powering the engines of bright quasars (Lynden-Bell 1969; Rees 1984). Quasars are one of the most luminous sources in the entire Universe, often outshining the whole light emitted from the galaxies hosting them. Their large radiative power means that we can observe quasars out to very high redshifts (Fan et al. 2006; Mortlock et al. 2011) and thus probe their evolution over more than 90 per cent of cosmic time. Whereas for quasars at $z \sim 6$–7 (Willott et al. 2010; De Rosa et al. 2011) the range of luminosities probed is still relatively narrow, for $z \lesssim 5$ the consensus on quasar luminosities is more complete thanks to both optical and X-ray surveys, such as Sloan Digital Sky Survey (SDSS), Great Observatories Origins Deep Survey (GOODS), Cosmological Evolution Survey (COSMOS) and *Chandra Deep Field*-North and -South.

While it is imperative for any state-of-the-art cosmological simulation to compare against this wealth of data, the study of supermassive black holes involves some broader and more fundamental questions. In a series of seminal theoretical papers (Haehnelt, Natarajan

★E-mail: deboras@ast.cam.ac.uk
†Hubble Fellow.

Published by Oxford University Press on behalf of the Royal Astronomical Society

& Rees 1998; Silk & Rees 1998; Fabian & Iwasawa 1999; King 2003) principal ideas have been developed to explain the possible mutual feedback between galaxies and their central black holes. Observational evidence for this physical relationship has been mounting over the years (Magorrian et al. 1998; Ferrarese & Merritt 2000; Tremaine et al. 2002; Marconi & Hunt 2003; Häring & Rix 2004; Gültekin et al. 2009; Gebhardt et al. 2011; Kormendy & Ho 2013; McConnell & Ma 2013), indicating that black hole masses correlate with host galaxy stellar properties, such as bulge luminosity, mass and velocity dispersion. Although these scaling relations may suggest that galaxies and black holes co-evolve, they are subject to many biases and systematic uncertainties both at the low mass and the massive end. Indeed recent work by McConnell & Ma (2013) and Kormendy & Ho (2013) revised significantly the $M_{\rm BH}$–$M_{\rm bulge}$ and $M_{\rm BH}$–σ relations (see also Gebhardt et al. 2011), such that for a given bulge mass or velocity dispersion, the best-fitting black hole masses are a factor of 2–3 higher than previously thought. These studies further highlighted that galaxies with different properties, e.g. pseudo-bulges versus real bulges, or cored versus power-law ellipticals, may correlate differently with their central black hole masses. Uncertainties in the origin of the black hole–galaxy scaling relations prompted some authors (Peng 2007; Hirschmann et al. 2010; Jahnke & Macciò 2011) to consider mass averaging in mergers as a root cause of scaling relations without the need to invoke any feedback. In this scenario repeated galaxy–galaxy and thus black hole–black hole mergers lead to the establishment of the $M_{\rm BH}$–$M_{\rm bulge}$ relation thanks to the central limit theorem.

One of the clues that could help shed light on the relative importance of feedback versus merger averaging is the redshift evolution of the black hole–galaxy scaling relations. While different observational pieces of evidence indicate that the scaling relation should evolve such that, for a given host galaxy at higher redshifts, black holes are more massive than their $z = 0$ counterparts (e.g. Treu, Malkan & Blandford 2004; Shields et al. 2006; Woo et al. 2008; Merloni et al. 2010, for a review see Kormendy & Ho 2013), systematic uncertainties, selection effects and insufficient data do not allow yet to conclude anything secure about the redshift evolution of the scatter. Thus from the observational point of view this remains an unsettled point, even though there is accumulating evidence for active galactic nuclei (AGN)-driven large-scale outflows (Cicone et al. 2012, 2014; Maiolino et al. 2012; Genzel et al. 2014b).

It is therefore of fundamental importance to understand from a theoretical point of view if indeed feedback from supermassive black holes affects their hosts significantly and if this leads to the co-evolutionary picture. The majority of past work based on mergers of isolated galaxies found that black holes play a crucial role in the morphological transformation of host galaxies and in the quenching of their star formation rates (for early works see e.g. Di Matteo, Springel & Hernquist 2005; Springel, Di Matteo & Hernquist 2005; Robertson et al. 2006) and that feedback from accreting black holes is responsible for the existence of the black hole–galaxy scaling relations. Based on these simulation results Hopkins et al. (2006) proposed a unified model for the merger-driven origin of quasars and their host spheroids. While this picture is theoretically appealing, fully self-consistent cosmological simulations indicate that galaxies and thus very likely their central black holes as well assemble through a variety of physical processes and not major mergers alone. Moreover, observations have thus far been inconclusive in showing a clear link between enhanced star formation rates of galaxies and AGN nuclear activity (see Azadi et al. 2015, and references therein), thus questioning the merger-driven co-evolution of the two.

The first cosmological simulations (Sijacki et al. 2007; Di Matteo et al. 2008) to investigate the black hole–galaxy co-evolution confirmed that AGN-driven outflows not only lead to black hole self-regulation but also to the establishment of the scaling relations, as isolated galaxy merger studies have advocated. These results were further confirmed by several independent groups and more recent simulations (Booth & Schaye 2009; Dubois et al. 2012; Hirschmann et al. 2014; Khandai et al. 2015; Schaye et al. 2015). What however still remains unclear is whether black hole–galaxy co-evolution occurs for all galaxies hosting supermassive black holes at their core or whether different galaxy types exhibit weaker or stronger physical links with their black holes. The main reason why this question remained unanswered theoretically until now stems from the difficulty to simulate representative galaxy samples covering the observed range of morphologies. Simulated galaxies typically appeared too centrally concentrated, formed too many stars and lacked sufficient rotational support. This has been one of the long standing issues in computational galaxy formation which even led some to question the Λ cold dark matter (ΛCDM) cosmology (e.g. Sommer-Larsen & Dolgov 2001). Now we understand that this was caused by insufficient numerical resolution, hydro solver inaccuracies and lack of modelling of the necessary physics. Only recently several simulation efforts (Guedes et al. 2011; Aumer et al. 2013; Stinson et al. 2013; Hopkins et al. 2014; Marinacci, Pakmor & Springel 2014), mostly based on the zoom-in technique of individual objects, have started reproducing extended, disc-dominated galaxies which in some aspects resemble our own Milky Way. Nonetheless, to study the black hole–galaxy co-evolution large-scale cosmological simulations are needed to have a sufficiently representative sample of objects. At the same time good spatial resolution is necessary to resolve at least the basic structural properties of galaxies hosting supermassive black holes. These conditions pose very challenging requirements on the dynamical range cosmological simulation should resolve.

The Illustris simulation project (Vogelsberger et al. 2014a, see also Genel et al. 2014a; Vogelsberger et al. 2014b) is the first cosmological simulation that is able to probe the necessary range of spatial scales with a comprehensive set of physical processes so that we can study black hole–galaxy co-evolution with unprecedented detail. This means that we not only have a statistically large and representative sample of objects from $z \sim 4$ to $z = 0$, but also that we can start to disentangle the physical link between black holes and their host galaxies as a function of galaxy morphology and colour. We anticipate here that this will allow us to pin down the most likely physics which is responsible for the establishment of the mutual feedback between galaxies and their central black holes, but we also highlight for which types of galaxies this feedback loop is not fully operational.

This paper is organized as follows. In Section 2 we outline our methodology, summarizing the numerical technique adopted, simulation characteristics and physics implementation. In Section 3.1 and in Appendix we discuss the convergence properties of the black hole model, while in Sections 3.2 and 3.3 we present the basic black hole properties, namely the cosmic black hole accretion rate and mass density as well as the mass function at $z = 0$. Section 3.4 summarizes the main results regarding the scaling relations of galaxies and their central black holes. We further discuss black hole Eddington ratios, AGN luminosity functions and cosmic downsizing in Sections 3.5 and 3.6, while in Section 3.7 we examine the link between star formation rate and nuclear AGN triggering. We finally discuss our results and draw conclusions in Section 4.

2 METHODOLOGY

2.1 Numerical method

In this study we use a series of large-scale cosmological simulations, the so-called Illustris project,[1] to investigate the link between black holes and their host galaxies across cosmic time. The Illustris simulations have been performed with the massively parallel hydrodynamical code AREPO (Springel 2010), which adopts a TreePM solver for gravity and a second-order accurate unsplit Godunov method for the hydro forces. The hydrodynamics equations are solved on an unstructured Voronoi mesh, which is allowed to freely move with the fluid in a quasi-Lagrangian fashion. The code has been thoroughly tested and validated on a number of computational problems and small-scale cosmological simulations (Springel 2010, 2011; Bauer & Springel 2012; Kereš et al. 2012; Sijacki et al. 2012; Torrey et al. 2012; Vogelsberger et al. 2012; Genel et al. 2013; Nelson et al. 2013) demonstrating excellent shock capturing properties, proper development of fluid instabilities, low numerical diffusivity and Galilean invariance, making it thus well posed to tackle the problem of galaxy formation.

2.2 The simulation suite

The Illustris simulation suite consists of large-scale cosmological simulations in a periodic box with 106.5 Mpc on a side, simulated with different physics and at different resolutions. A standard, flat ΛCDM cosmology is assumed with $\Omega_{\rm m,0} = 0.2726$, $\Omega_{\Lambda,0} = 0.7274$, $\Omega_{\rm b,0} = 0.0456$, $\sigma_8 = 0.809$, $n_{\rm s} = 0.963$ and $H_0 = 70.4\,{\rm km\,s^{-1}\,Mpc^{-1}}$ consistent with the *Wilkinson Microwave Anisotropy Probe* 9-year data release (Hinshaw et al. 2013). The starting redshift of the simulations is $z = 127$ and all simulations have been evolved to $z = 0$. The physics included ranges from dark matter only simulations (Illustris-Dark), non-radiative hydrodynamical simulations (Illustris-NR), to simulations with the full galaxy formation physics module switched on (Illustris) which will be used in this study. The simulations have been performed at three different resolutions. (1) Low-resolution box with 3×455^3 dark matter, gas and Monte Carlo tracer resolution elements, a typical gas cell mass of $m_{\rm gas} = 8.05 \times 10^7\,{\rm M}_{\odot}$, dark matter particle mass of $m_{\rm DM} = 4.01 \times 10^8\,{\rm M}_{\odot}$ and gravitational softenings[2] $\epsilon_{\rm gas} = 2.84$ kpc and $\epsilon_{\rm DM} = 5.86$ kpc. (2) Intermediate-resolution box with 3×910^3 resolution elements in total, $m_{\rm gas} = 1.01 \times 10^7\,{\rm M}_{\odot}$, $m_{\rm DM} = 5.01 \times 10^7\,{\rm M}_{\odot}$, $\epsilon_{\rm gas} = 1.42$ kpc and $\epsilon_{\rm DM} = 2.84$ kpc. (3) High-resolution box with 3×1820^3 resolution elements in total, $m_{\rm gas} = 1.26 \times 10^6\,{\rm M}_{\odot}$, $m_{\rm DM} = 6.26 \times 10^6\,{\rm M}_{\odot}$, $\epsilon_{\rm gas} = 0.71$ kpc and $\epsilon_{\rm DM} = 1.42$ kpc. For further details of the simulations see Vogelsberger et al. (2014b) and Genel et al. (2014a). In this study we will mainly focus on the highest resolution box of Illustris, which we call henceforth Illustris for brevity, while we will take advantage of the lower resolution boxes when exploring the convergence issues.

2.3 The model for galaxy formation

The Illustris simulations contain a comprehensive array of modules that describe galaxy formation physics beyond non-radiative processes. This includes primordial and metal-line cooling in the presence of time-dependent ultraviolet background (Faucher-Giguère et al. 2009) including gas self-shielding (Rahmati et al. 2013), where the metals are naturally advected with the fluid flow; a subgrid model for star formation and associated supernovae feedback as in Springel & Hernquist (2003) adopting a softer equation of state (Springel et al. 2005) with $q = 0.3$ and a Chabrier initial mass function (Chabrier 2003); a model for stellar evolution, gas recycling, metal enrichment (see also Wiersma et al. 2009) and mass- and metal-loaded galactic outflows, where the wind mass loading scales with the inverse of the wind velocity squared, motivated by energy conservation arguments (see also Oppenheimer & Davé 2008; Okamoto et al. 2010; Puchwein & Springel 2013); and a model for black hole seeding, accretion and feedback that we will describe in more detail in Section 2.4. A full account of these prescriptions is given in our pilot study (Vogelsberger et al. 2013; Torrey et al. 2014) where the basic properties of galaxies are compared with observables. Specifically, given that currently it is not possible to describe the physics of star formation and black holes in an ab initio manner, simple phenomenological and empirical subgrid models need to be employed if we are to gain insight into the physics of galaxy formation. In the Illustris project the free parameters of the subgrid models are set to physically plausible values which have been fixed after calibrating the simulations against a few fundamental observables, such as the cosmic star formation rate history and the stellar mass function at $z = 0$. This calibration has been performed on smaller cosmological boxes with 35.5 Mpc on a side and is presented in Vogelsberger et al. (2013) and Torrey et al. (2014).

[1] http://www.illustris-project.org

[2] Note that the gravitational softenings are Plummer equivalent.

2.4 Black hole model

2.4.1 Black hole accretion

In the Illustris simulations collisionless black hole particles with a seed mass of $1.42 \times 10^5\,{\rm M}_{\odot}$ ($10^5\,h^{-1}\,{\rm M}_{\odot}$) are placed with the aid of the on-the-fly friends-of-friends (FOF) algorithm in all haloes more massive than $7.1 \times 10^{10}\,{\rm M}_{\odot}$ that do not contain a black hole particle already. Thereafter, the black hole seeds can grow in mass either through gas accretion, which we parametrize in terms of Eddington limited Bondi–Hoyle–Lyttleton-like accretion (for further details see Di Matteo et al. 2005; Springel et al. 2005), or via mergers with other black holes. At $z = 4$ our high-resolution Illustris simulation already tracks 9414 black holes, at $z = 2$ this number more than doubles leading to 24 878 black holes in total, while at $z = 0$ there are 32 542 black holes in total with 3965 black holes more massive than $10^7\,{\rm M}_{\odot}$.

With respect to our previous work (e.g. Springel, Di Matteo & Hernquist 2005; Sijacki et al. 2007; Sijacki, Springel & Haehnelt 2009) there are a few updates in the black hole model that we list here. First, we do not take the relative velocity of black holes with respect to their surrounding gas into account when estimating Bondi–Hoyle–Lyttleton-like accretion and we merge black hole pairs which are within smoothing lengths of each other irrespective of their relative velocity. This is motivated by the fact that we use a repositioning scheme to ensure that the black hole particles are at the gravitational potential minimum of the host haloes and do not spuriously wander around due to two body scattering effects with massive dark matter or star particles. This leads to ill-defined black hole velocities. Note however that our estimated sound speeds entering Bondi–Hoyle–Lyttleton-like accretion are typically larger than the relative velocity term, so that the black hole accretion rates are not affected significantly by this update. Moreover, during accretion events we gradually drain the parent gas cell of its mass rather than stochastically swallowing one of the neighbouring gas cells. We also use the parent gas cell to estimate the gas density instead of performing a kernel weighted average over gas neighbours, as we have done in the past. Finally, we introduce a black hole 'pressure criterion' whereby the accretion rate estimate is lowered in cases where the gas pressure of the ambient medium cannot compress gas to a density exceeding the star formation threshold in the vicinity of an accreting black hole. Here the $\alpha = 100$ pre-factor in the Bondi prescription needed to compensate for the unresolved cold and hot clouds of our subgrid interstellar medium model becomes superfluous and could lead to the formation of an unphysically large and hot gas bubble around massive black holes accreting from a low-density medium. For further details on the 'pressure criterion' see Vogelsberger et al. (2013). Note that self-regulated growth of black holes is largely unaffected by this change.

2.4.2 *Black hole feedback*

As for the black hole feedback we consider three different modes: 'quasar', 'radio' and 'radiative' feedback. In the 'quasar' mode AGN bolometric luminosity is computed directly from the black hole accretion rate assuming a given radiative efficiency. A small fraction of the AGN bolometric luminosity is thermally coupled to the surrounding gas with an efficiency factor of $\epsilon_{\rm f} = 0.05$ thus effectively leading to an energy-driven outflow in the case of negligible radiative losses.[3] The switch between 'quasar' and 'radio' mode is determined by the black hole Eddington ratio following Sijacki et al. (2007). In the 'radio' mode hot bubbles are randomly placed within a sphere around each black hole. For all active black hole particles we estimate the local gas density at the position of the bubble. We then use the analytic cocoon expansion equation (see equation 5 in Sijacki et al. 2007) to rescale both the radii of the bubbles and the radii of the spheres within which the bubbles are created from the initially set default values. The thermal energy injected into the bubbles is directly linked to the black hole mass growth via radiative efficiency and thermal coupling efficiency in the radio mode, $\epsilon_{\rm m}$ (see equation 4 in Sijacki et al. 2007).

With respect to the original work by Sijacki et al. (2007) we change the values of some of the model parameters. The scaling of the radius of the sphere within which bubbles are injected has been increased from 60 to 100 kpc. With a larger radius the energy contrast between the bubbles and the surrounding gas can be higher and thus lead to larger feedback effects. Note however given that for each black hole we scale this radius according to the analytic cocoon expansion equation, thus this change in scaling is not very significant.

We further make two more significant changes: we increase the efficiency factor of thermal coupling, $\epsilon_{\rm m}$, from 0.2 to 0.35 and we increase the Eddington ratio threshold, $\chi_{\rm radio}$, below which the 'radio' mode feedback kicks in from 0.01 to 0.05. These two changes have been motivated by the above-mentioned calibration against the observed cosmic star formation rate history and the $z = 0$ stellar mass function. We find that a higher $\epsilon_{\rm m}$ value is needed to sufficiently suppress star formation in massive galaxies which tends to be even higher than in previous work due to several factors: (i) stellar mass loss and metal-line cooling, which can affect the cosmic star formation rate density significantly (e.g. see fig. 15 in Vogelsberger et al. 2013); (ii) more accurate gas cooling in AREPO with respect to standard smoothed particle hydrodynamics (SPH). This is due to the much more effective gas mixing (see e.g. Sijacki et al. 2012; Torrey et al. 2012) which becomes even more important when considering mixing of metal-enriched galactic winds with the hot, diffuse halo. Also, it has been shown (Bauer & Springel 2012; Vogelsberger et al. 2012) that in AREPO there is no heating of gas due to artificial dissipation of subsonic turbulence, as is the case in the standard SPH, which may affect cooling rates as well (Nelson et al. 2013). The higher Eddington ratio threshold value leads to more efficient 'radio' mode feedback being active in somewhat lower mass galaxies and at higher redshifts as well which helps reproducing the 'knee' of the $z = 0$ stellar mass function.

In addition to the 'quasar' and 'radio' mode, we also take into account 'radiative' feedback where we modify the net cooling rate of gas (namely, photoionization and photoheating rates) in the presence of strong ionizing radiation emanating from actively accreting black holes. Assuming a fixed spectral energy distribution we consider gas below the density threshold for star formation to be in the optically thin regime and compute the bolometric intensity each gas cell experiences due to the AGN radiation field of all black holes within a given search radius which is set by a threshold in the ionization parameter and capped to three times the virial radius of the parent halo. Note that 'radiative' feedback is most effective for black holes in the 'quasar' mode accreting close to the Eddington limit.

While the quasar efficiency factor, $\epsilon_{\rm f}$, has been set by Springel et al. (2005) and Di Matteo et al. (2005) to match the normalization of the $M_{\rm BH}$–σ relation in the isolated galaxy mergers, note that none of the black hole model parameters has been tuned to match any of the black hole properties which hence can be viewed as genuine predictions of the model. For further details on the black hole model see Springel et al. (2005), Sijacki et al. (2007) and Vogelsberger et al. (2013).

We finally note that in Illustris the radiative efficiency has been set to $\epsilon_{\rm r} = 0.2$. This change from the standardly adopted value of 0.1 has been motivated by the findings of Yu & Tremaine (2002), where it has been shown that luminous quasars (which are the objects we are most interested in) should have $\epsilon_{\rm r} \sim 0.2$. In our model $\epsilon_{\rm r}$ is essentially unconstrained given that in all equations it is degenerate with the values of $\epsilon_{\rm f}$ and $\epsilon_{\rm m}$. The only equation where $\epsilon_{\rm r}$ enters on its own is the one that determines the fraction of the accreted mass lost to radiation, which however leads to a very small effect. Nonetheless, as we will show in Section 3.6, taking together the results regarding black hole mass and luminosity functions we can place interesting constraints on the average radiative efficiency of AGN.

3 RESULTS

3.1 Convergence issues

We start our analysis by looking at the convergence properties of our galaxy formation model. Here we are specifically interested in the basic black hole properties, while the convergence of other quantities has been discussed in Vogelsberger et al. (2013), Torrey et al. (2014) and Genel et al. (2014a). In Fig. 1 we show the cosmic star formation rate density and black hole accretion rate density (left-hand panel), as well as stellar and black hole mass density (right-hand panel), for the three different resolution Illustris simulations, as indicated in the legend. With higher resolution smaller mass galaxies are better resolved and this leads to an increase in the

[3] Note that once gas internal energy is increased due to black hole feedback, gas is allowed to radiatively cool and heat, except for the gas within the multiphase model for star formation that is colder than the effective temperature of our equation of state assumed there. The internal energy of this cold, multiphase gas is set to the effective energy of the multiphase model.

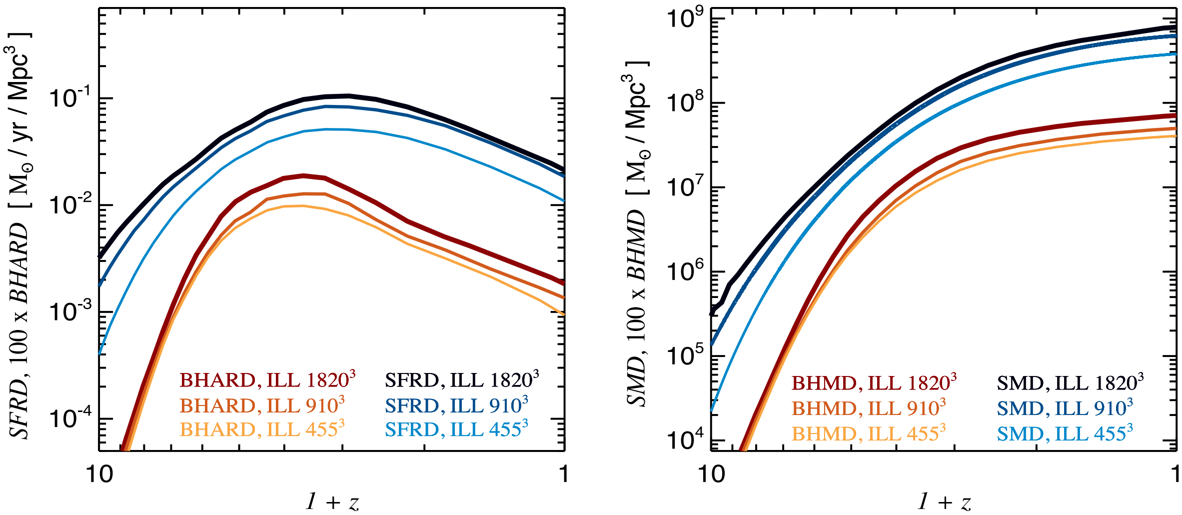

Figure 1. Left: time evolution of the star formation rate density (blue curves) and of the black hole accretion rate density (red curves; rescaled by a factor of a 100) for three different resolutions, as indicated on the legend. While the numerical convergence in the star formation rate density is very good, the black hole accretion rate density is not yet converged at the highest resolution. Note that the overall shape of the black hole accretion rate density is somewhat different than that of the star formation rate density, i.e. it rises faster at high redshifts and also peaks at a higher redshift $z \sim 2.5$–3. Right: stellar mass density and black hole mass density as a function of cosmic time for the same set of simulations.

star formation rate at high redshifts, which is especially pronounced between the low- and intermediate-resolution simulations. However, at lower redshifts, i.e. for $z < 5$, the bulk of star formation occurs in sufficiently well-resolved galaxies so that the total star formation rate density does not increase much with higher resolution. This is in particular true when we compare our intermediate-resolution simulation with the high-resolution run where both star formation rate density and stellar mass density exhibit excellent convergence properties.

The convergence properties of the black hole accretion rate and mass density are however somewhat poorer. Here for $z > 5$ the black hole accretion rate density is essentially the same in all three simulations, given that by this time it is dominated by low-mass black holes that have been relatively recently seeded within well-resolved dark matter haloes. At later times there is an approximately constant offset between both low versus intermediate and intermediate versus high resolution run (amounting to a factor of ~1.5). This indicates that the black hole accretion rate density is not yet fully converged even for our highest resolution simulation. We have investigated whether there are any clear trends in black hole accretion rate density convergence for different black hole mass ranges, and found that for $z > 2$ more massive black holes exhibit worse convergence, while for $z < 2$ the convergence rate is similar regardless of the black hole mass. Clearly this is a result that we need to keep in mind when interpreting our findings, but we anticipate here that the convergence properties of other quantities, such as, for example, the black hole mass function and the black hole mass–bulge mass relation, are still very good, as we discuss in Sections 3.3 and 3.4 and in the Appendix.

3.2 Black hole accretion rate and mass density

Focusing now on the shape of star formation and black hole accretion rate densities, shown in Figs 1 and 2, we note that the black hole accretion rate density rises more steeply at high redshifts, it has a sharper peak which occurs earlier ($z \sim 2.5$–3) and it also declines somewhat more steeply thereafter all the way to $z = 0$. Consequently, for $z < 2$ the total black hole mass density increases less with time than the total stellar mass density. This demonstrates that while globally there is a relation between star formation and black hole accretion rates in galaxies, these two processes are not necessarily intimately linked (see also e.g. Merloni 2004; Sijacki et al. 2007; Di Matteo et al. 2008; Merloni & Heinz 2008; Somerville et al. 2008), as we will discuss more in detail in Section 3.7.

In Fig. 2 we plot the total black hole accretion rate density (left-hand panel) and the black hole mass density (right-hand panel) for the highest resolution Illustris simulation, but now split by the black hole mass at a given redshift, as indicated on the legend. With decreasing redshift more massive black holes start to dominate the total black hole accretion rate density, except for the most massive black holes with $M_{\rm BH} > 10^9\,{\rm M}_{\odot}$, which however dominate the total black hole mass density for $z < 2$. Also, even though the black hole accretion rate density shapes are quite similar for the different black hole mass ranges considered, they peak at later times for more massive black holes. Given that the distribution of Eddington ratios is fairly flat as a function of black hole mass for $z \geq 1$ (for further details see Section 3.5), different peaks reflect the cosmic time when black holes of a given mass contribute most to the total black hole accretion rate density due to combination of their number density and accretion rate in absolute numbers. Note that for $z < 3$ and for $M_{\rm BH} > 10^8\,{\rm M}_{\odot}$ black holes typically enter the 'radio' mode feedback which is bursty, leading to significant and rapid variations in the black hole accretion rate density.

In the right-hand panel of Fig. 2 we also indicate with the shaded region the range of possible black hole mass densities derived from Soltan-type arguments where radiative efficiency is varied from 0.057 (top) to 0.4 (bottom), as reported by Volonteri (2010). New constraints from a compilation of AGN X-ray luminosity surveys by Ueda et al. (2014) are shown with black circles connected with a thick line. The Illustris result is in excellent agreement with observational findings from Ueda et al. (2014) and indicates that on

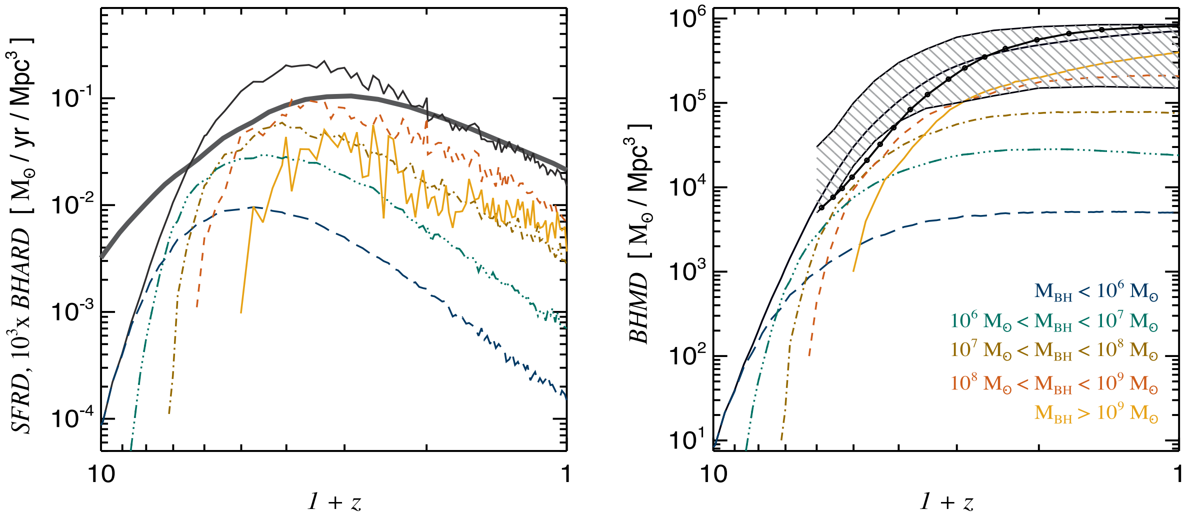

Figure 2. Left: time evolution of the star formation rate density (thick dark grey curve) and of the black hole accretion rate density (thin black curve; rescaled by a factor of a 1000) for the highest resolution Illustris simulation. Coloured lines (from blue to orange: dashed, triple-dot–dashed, dot–dashed, dashed and continuous) indicate total black hole accretion rate densities for black holes in a given range of masses, as indicated on the legend. With decreasing redshift more massive black holes dominate the total black hole accretion rate density, except for the most massive black holes with $M_{\rm BH} > 10^9\,{\rm M}_{\odot}$. Note that for $z < 3$ and for $M_{\rm BH} > 10^8\,{\rm M}_{\odot}$ there is a considerable 'noise' in the black hole accretion rate density. This is driven by black holes entering the 'radio' mode feedback which is bursty. Right: total black hole mass density (black thin line) for all black holes and split by the black hole mass bins (coloured lines from blue to orange with the same line styles as in the left-hand panel). The shaded region is the allowed range of mass densities where radiative efficiency is varied from 0.057 to 0.4, as reported by Volonteri (2010). Black circles connected with a thick line are for the new estimate from Ueda et al. (2014).

average radiative efficiencies of accreting black holes could be low. This is an interesting point that we will discuss more in detail in Section 3.6.

3.3 Black hole mass function

In Fig. 3 we show the redshift evolution of the black hole mass function at $z = 0$, 1, 2, 3 and 4 (left-hand panel) and the black hole mass function at $z = 0$ split by the Eddington ratios of black holes (right-hand panel), as indicated in the legend. In both panels we include all black holes irrespective of their mass or accretion rate. The hatched region marks the mass function estimate with the 1σ uncertainty from Shankar (2013), assuming the revised $M_{\rm BH}$–σ relation from McConnell & Ma (2013) and applying it to all local galaxies. The dotted region is the same but assuming Sa galaxies do not host any black hole (Shankar 2013). Note that this likely represents a lower bound on the black hole mass function. The Illustris black hole mass function at $z = 0$ agrees quite well with the estimate from Shankar (2013), except for the lowest mass black holes with $M_{\rm BH} < 10^7\,{\rm M}_{\odot}$. This agreement is particularly encouraging given that recently black hole scaling relations have been significantly revised (for further details see Kormendy & Ho 2013; McConnell & Ma 2013), where for a given e.g. bulge mass the best-fitting black hole mass is about a factor of 2–3 higher with respect to the estimates by Häring & Rix (2004) (we will discuss this further in Section 3.4). Note that, as we show in Appendix, the uncertainty due to the convergence of the black hole mass function for our different resolution runs is smaller than the observational uncertainty calculated by Shankar (2013). Moreover, for black holes with Eddington ratios $\lambda_{\rm EDD} > 10^{-4}$ the convergence rate in the mass function improves especially at the massive end (for further details see Appendix), thus indicating that rather than some minimum black hole mass a minimum accretion rate is needed for the model to converge better. The disagreement between the Shankar (2013) results and the Illustris predictions at the low-mass end, i.e. for $M_{\rm BH} < 10^7\,{\rm M}_{\odot}$, could be caused by a number of reasons. Observational uncertainties increase for low-mass black holes, and at the same time our simulation results are also least reliable at the low-mass end. Here, additionally to numerical convergence issues, the black hole number densities and masses are most dependent on our rather simplistic seeding prescriptions and on the initial growth before the self-regulation is achieved. Regarding the seeding prescription three issues arise: (i) the choice of the black hole seed mass which in our model is fairly large, i.e. $M_{\rm BH,seed} = 10^5\,h^{-1}\,{\rm M}_{\odot}$; (ii) the fact that we seed all haloes above a certain mass regardless of redshift or any other halo property, for example, such as the gas metallicity and (iii) the fact that due to the black hole repositioning, haloes that temporarily become part of a larger FOF group are likely to lose their central black holes prematurely and if above mass threshold will be re-seeded with a new black hole.

The left-hand panel of Fig. 3 shows how the black hole mass function gradually builds up with cosmic time. The first $10^9\,{\rm M}_{\odot}$ black holes are already in place before $z = 4$, while ultramassive black holes with $\sim 10^{10}\,{\rm M}_{\odot}$ form at $z < 2$. Note that the Illustris volume of $(106.5\,{\rm Mpc})^3$ is too small, by a factor of ~ 300 at least, to contain very massive black holes at $z = 6$ which are thought to be powering high-redshift quasars (Sijacki et al. 2009; Costa et al. 2014a) and is thus unsuitable for studying these rare objects. At the low-mass end, i.e. for $M_{\rm BH} < 10^7\,{\rm M}_{\odot}$ the mass function does not evolve significantly after $z \sim 2$, while for $M_{\rm BH} < 2 \times 10^9\,{\rm M}_{\odot}$ the mass function does not change much for $z < 1$. At the massive end, i.e. for $M_{\rm BH} > 2 \times 10^9\,{\rm M}_{\odot}$ there is always evolution due to the residual 'hot mode' accretion and black hole–black hole mergers. To study the downsizing properties of the black hole population it is thus much more straightforward to analyse (hard X-ray) luminosity functions, as we discuss in Section 3.6.

In the right-hand panel of Fig. 3 we split the Illustris black hole mass function by the Eddington ratios of black holes, which demonstrates that in the mean Eddington ratios are moderate (see also Section 3.5). At the massive end, i.e. for $M_{\rm BH} > 10^9\,{\rm M}_{\odot}$ Eddington

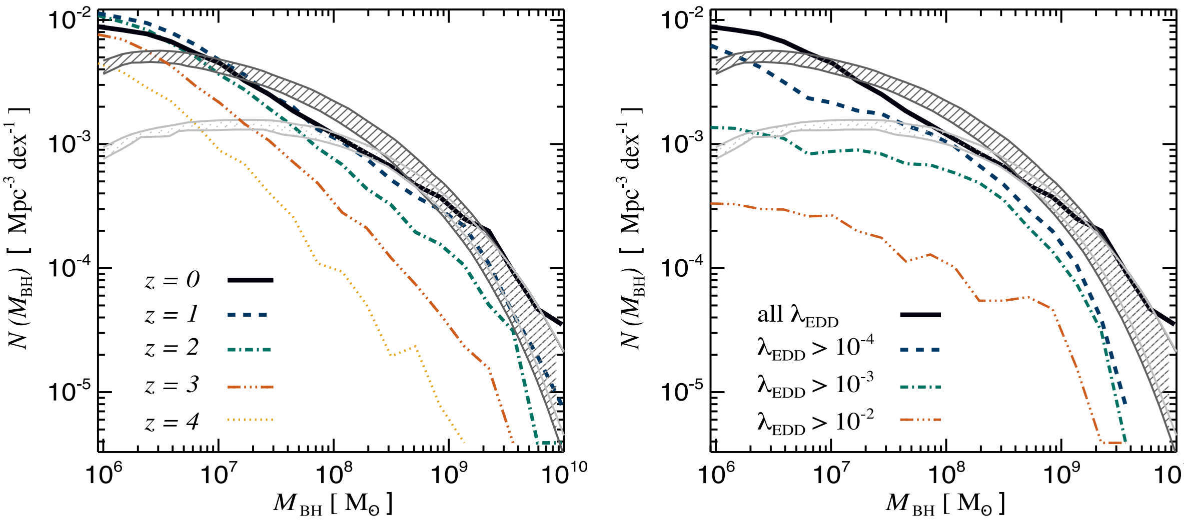

Figure 3. Left: black hole mass function at $z = 4$, 3, 2, 1 and 0 for all black holes in the simulated volume. The hatched region is the mass function estimate with 1σ uncertainty from Shankar (2013), assuming the revised $M_{\rm BH}$–σ relation from McConnell & Ma (2013) and applying it to all local galaxies. The dotted region is the same but assuming Sa galaxies do not host any black holes. In Illustris the black hole mass function gradually builds up with cosmic time: at the low-mass end, i.e. for $M_{\rm BH} < 10^7\,{\rm M}_\odot$ the mass function does not change much for $z < 2$, for $M_{\rm BH} < 2 \times 10^9\,{\rm M}_\odot$ the mass function does not change much for $z < 1$, while at the massive end there is always evolution due to the residual 'hot mode' accretion and black hole–black hole mergers. Right: black hole mass function at $z = 0$, split by the Eddington ratios of black holes, as indicated on the legend. It is clear that in the mean the Eddington ratios are moderate, but they are especially low at the massive end where black holes are in the radiatively inefficient accretion regime.

ratios plummet indicating that these black holes are in a radiatively inefficient accretion regime, as expected from the observed scarcity of luminous quasars in the local Universe. For $M_{\rm BH} \sim 10^8\,{\rm M}_\odot$ almost all black holes have $\lambda_{\rm EDD} > 10^{-4}$, while towards lower masses there is an increasing number of black holes with very low Eddington ratios.

3.4 Scaling relations with host galaxies and their evolution

3.4.1 $\mathrm{M_{BH}}$–$\mathrm{M_{bulge}}$ *relation at* $z = 0$

In Fig. 4 we show the Illustris prediction for the black hole mass–stellar bulge mass relation. Here the total stellar mass within the stellar half-mass radius has been adopted as a proxy for the bulge mass. Note that we do not morphologically distinguish between the real bulges and pseudo-bulges but we do split galaxies into different categories based on their colours.[4] Furthermore, from now on we take into account all galaxies hosting supermassive black holes with stellar half-mass greater than $10^8\,{\rm M}_\odot$ and we refer to the $M_{\rm BH}$–$M_{\rm bulge}$ relation of the whole population, even though many of these galaxies might not contain a real bulge or might be effectively bulgeless. The colour coding in Fig. 4 is according to the $g - r$ colours of host galaxies and we consider only the central galaxies of each FOF halo (i.e. the main subhalo of each FOF halo that contains at least one black hole particle) thus excluding the satellites from this analysis. For each subhalo, in case it contains multiple black holes, we select the black hole that is closest to the centre of the subhalo (defined as the position of the most bound particle). We have also repeated the analysis selecting the most massive black hole of each subhalo and this does not lead to any significant difference.

[4] Morphologically or kinematically based definitions of bulge masses might lead to somewhat different results if, for example, the bulge mass fractions depend strongly on the stellar mass, but this analysis is beyond the scope of this paper.

The thick black line in Fig. 4 denotes the best-fitting $M_{\rm BH}$–$M_{\rm bulge}$ relation from a recent compilation by Kormendy & Ho (2013) fitted to ellipticals and spirals with bulges only. Symbols with error bars are from Kormendy & Ho (2013) as well, where circles are for ellipticals, stars are for spirals with a bulge and squares are for pseudo-bulges. As mentioned in Section 3.3, the black hole mass–host galaxy relations have been recently significantly revised (see e.g. Gebhardt et al. 2011; Kormendy & Ho 2013; McConnell & Ma 2013) and the best-fitting black hole mass is a factor 2–3 higher than previously estimated (Häring & Rix 2004), thus it is important to compare against the newest observational findings.

The agreement between the Illustris result and the observations is very good, in particular taking into account that the best-fitting observed relation is for ellipticals and bulges only and that our quenched galaxies lie exactly on this relation. The result not only reproduces the slope and the normalization of the observed $M_{\rm BH}$–$M_{\rm bulge}$ relation, but qualitatively also matches the colours and the morphologies of galaxies on this relation in agreement with the morphological split performed by Kormendy & Ho (2013). This is the first time, to our knowledge, that such a wealth of properties of galaxies hosting supermassive black holes is predicted by self-consistent cosmological simulations of galaxy formation. Furthermore, this implies that with the Illustris simulations we can not only study how black holes and galaxies co-evolve in the mean, but also we can gain a much deeper insight into which galaxy types are strongly physically linked with their central black holes and which are much less affected by the presence of a supermassive black hole in their centre. This seems to be the case, for example, for the pseudo-bulges which correspond to the simulated blue star-forming galaxies below the best-fitting $M_{\rm BH}$–$M_{\rm bulge}$ relation as we discuss below.

Specifically, by focusing on the massive black hole end, i.e. for $M_{\rm BH} > 10^9\,{\rm M}_\odot$, the simulated host galaxies are very red with $g - r$ colours greater than 0.7 and the typical morphologies resemble ellipticals, which have strong central light concentrations, extended

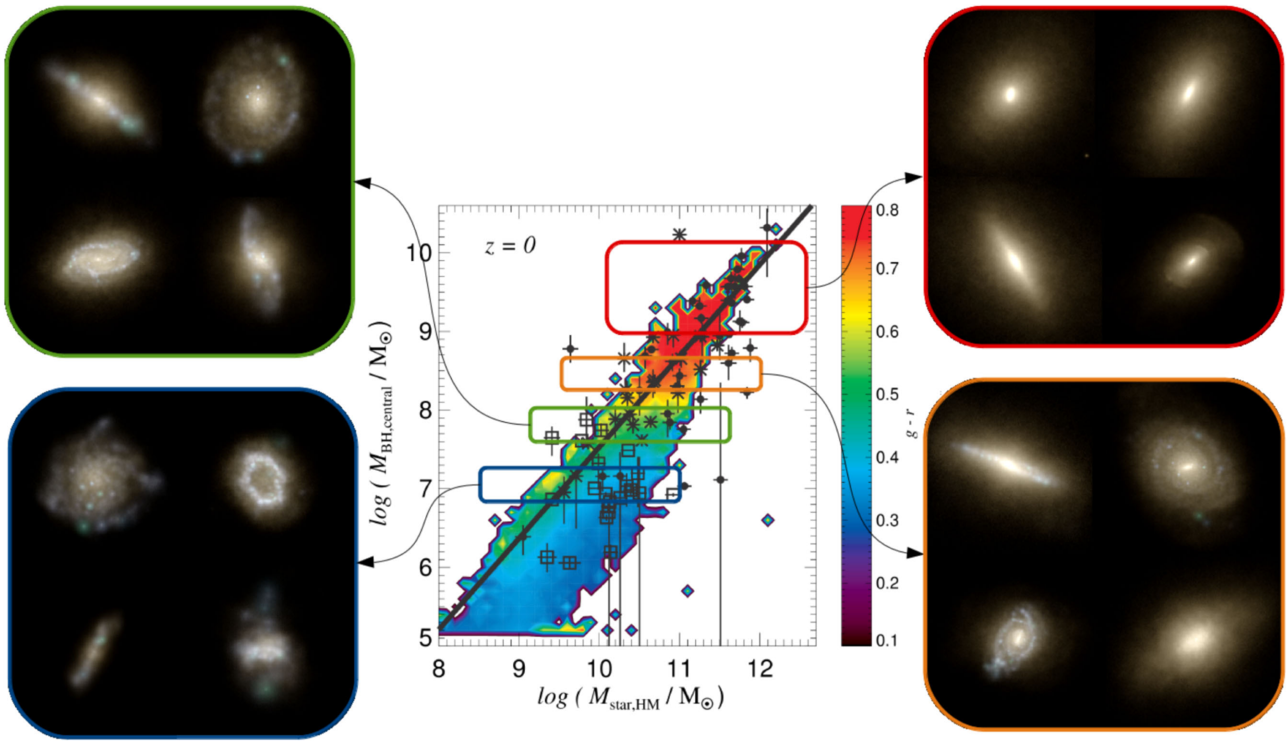

Figure 4. Central panel: stellar half-mass of all galaxies at $z = 0$ versus their central black hole mass. Colour coding is according to the $g - r$ colours of galaxies. The thick black line denotes the best-fitting $M_{\rm BH}$–$M_{\rm star,\,HM}$ relation from Kormendy & Ho (2013) fitted to ellipticals and galaxies with bulges only. Symbols with error bars are from Kormendy & Ho (2013) as well, where circles are for ellipticals, stars are for spirals with a bulge and squares are for pseudo-bulges. Overall, our simulation reproduces the observed findings very well. Note that for $M_{\rm star,\,HM} \lesssim 10^{11}\,{\rm M}_\odot$ the simulated black holes which are above the best-fitting observed relation live in redder galaxies, indicating feedback from these black holes is quenching their hosts more efficiently. Four side panels: stellar morphologies of galaxies visualized using SDSS g, r and i bands (Torrey et al. 2015) selected within a range of black hole masses, as indicated by the coloured boxes. While for all four black hole mass ranges there is a morphological mix of host galaxies, lower mass black holes are preferentially hosted in bluer star-forming and more disc-dominated galaxies.

red envelopes, post-merger shells and sometimes red discs, as illustrated in the top right-hand side panel. As we move along the $M_{\rm BH}$–$M_{\rm bulge}$ relation towards black holes with masses of a few $10^8\,{\rm M}_\odot$, typical $g - r$ colours are 0.65 and the host galaxies exhibit more of a morphological mix with some red spheroidal galaxies, quenched extended discs, as well as blue star-forming discs but with prominent red bulges (see bottom right-hand side panel). For $\sim 10^8\,{\rm M}_\odot$ black holes this transition is more evident with host galaxies lying in the so-called 'green valley' (Schawinski et al. 2014), with mean $g - r$ colours of 0.5 and morphologies showing both a red quenched population and blue star-forming discs which are sometimes tilted with respect to the old stellar population indicating a different assembly history (see top left-hand side panel). It is interesting to note that the black holes in 'green valley' galaxies are the most efficient accretors (see Section 3.3) and this likely leads to the rapid transition between star-forming and quenched populations. Finally, for black hole masses $\leq 10^7\,{\rm M}_\odot$, the majority of hosts are blue and star forming with $g - r$ colours of 0.3–0.4 and irregular and perturbed morphologies (see bottom left-hand side panel).

While in general host galaxy colours change from blue to red with increasing black hole mass, note that for $M_{\rm star,\,HM} \lesssim 10^{11}\,{\rm M}_\odot$ simulated black holes which are above the best-fitting observed relation live in redder galaxies. This indicates that the feedback from these black holes, which are more massive than the average $M_{\rm BH}$ at a given $M_{\rm bulge}$, is quenching their hosts more efficiently. Conversely, black holes that are undermassive for their host bulge mass (again for $M_{\rm star,\,HM} \lesssim 10^{11}\,{\rm M}_\odot$) tend to live in the bluest galaxies, which are least affected by their feedback. The same conclusion has been reached in a recent paper by Snyder et al. (2015), where it has been also shown that at a fixed halo mass galaxies with above-average black hole masses have below-average stellar masses and earlier-than-average morphological types.

We finally note that the scatter in the simulated $M_{\rm BH}$–$M_{\rm bulge}$ relation becomes smaller with higher black hole mass. This trend is also in accordance with observational findings. The reasons for this are twofold: (i) as the black holes become more massive and reach certain critical mass (King 2003; Springel, Di Matteo & Hernquist 2005; Costa, Sijacki & Haehnelt 2014b) their feedback is sufficiently strong to self-regulate not only the black hole mass itself but also the properties of their host galaxy; (ii) for higher black hole masses more galaxy–galaxy dry mergers and thus black hole–black hole mergers happen and due to the central limit theorem (Peng 2007; Hirschmann et al. 2010; Jahnke & Macciò 2011), the scatter in $M_{\rm BH}$–$M_{\rm bulge}$ tightens. We emphasize here that black hole feedback is still a necessary and crucial ingredient to reproduce the $M_{\rm BH}$–$M_{\rm bulge}$ relation and that this establishes a physical link between the black holes and their central galaxies.

3.4.2 *Redshift evolution of the* $M_{\rm BH}$–$M_{\rm bulge}$ *relation*

In Fig. 5 we show the simulated $M_{\rm BH}$–$M_{\rm bulge}$ relation at $z = 1$, 2, 3 and 4. Colour coding is now according to the black hole bolometric luminosity. The solid line is the fit from Kormendy & Ho (2013)

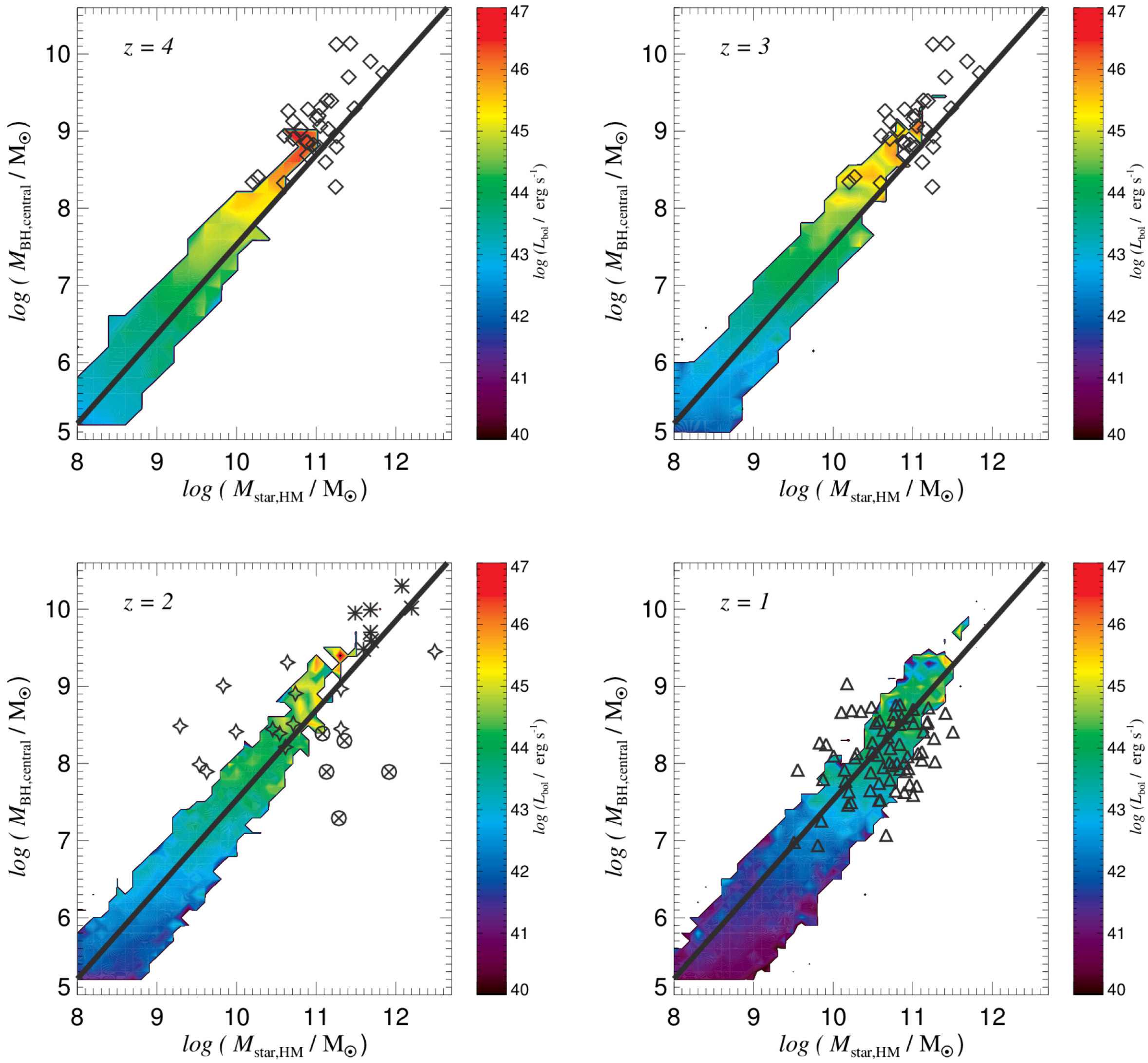

Figure 5. Redshift evolution of the black hole mass–stellar bulge mass relation at $z = 4$, 3, 2 and 1. Illustris results are shown as 2D histograms, where colour coding is according to the black hole bolometric luminosity (contours include all black holes). Data points at different redshifts are from Kormendy & Ho (2013) (see text for more details and their fig. 38), while the solid line is the fit from Kormendy & Ho (2013) to $z = 0$ ellipticals and bulges, as in Fig. 4. Simulation results are consistent with data points at all redshifts and indicate evolution mostly in the normalization of the best-fitting relation.

to $z = 0$ ellipticals and bulges, as in Fig. 4, which we plot to emphasize the evolution of the simulated $M_{\rm BH}$–$M_{\rm bulge}$ relation. Data points at different redshifts are from Kormendy & Ho (2013), with triangles corresponding to AGN ($z = 0.1$–1), stars to radio galaxies (RGs; $z \sim 2$), circles with a cross to submillimetre galaxies (SMGs; $z \sim 2$), starred diamonds to low-redshift quasars (QSOs; $z = 1$–2) and diamonds to high-redshift QSOs ($z = 2$–4).[5] Simulation results are in generally good agreement with the observations. Nonetheless, due to the limited box size we can probe neither the very luminous nor the very rare objects, so we cannot conclude much about the evolution of the $M_{\rm BH}$–$M_{\rm bulge}$ relation at the very massive end or about whether the relatively large scatter seen in observations especially for the SMGs is reproduced (but see also Sparre et al. 2015 who find a too low fraction of starbursts in Illustris). We do however find a trend for the simulated black holes to be more massive for their bulge host mass at higher redshift (see also recent observational work by Bongiorno et al. 2014 who find a similar trend in agreement with Merloni et al. 2010, and Schulze & Wisotzki 2014 who instead find no evidence for evolution). This is quantified in Table 1, where we list the best-fitting slope and normalization of the simulated

Table 1. The best-fitting simulated $\log(M_{\rm BH}/{\rm M}_\odot) = A\log(M_{\rm bulge}/{\rm M}_\odot) + B$ relation from $z = 0$ to 4, where A is the slope and B the normalization. Here we take into account only black holes hosted by galaxies with stellar half-mass greater than 10^8 M$_\odot$.

Redshift	Slope	Normalization
$z = 0$	1.21	−5.29
$z = 1$	1.23	−5.07
$z = 2$	1.23	−4.85
$z = 3$	1.25	−4.91
$z = 4$	1.28	−5.04

[5] See also fig. 38 of Kormendy & Ho (2013).

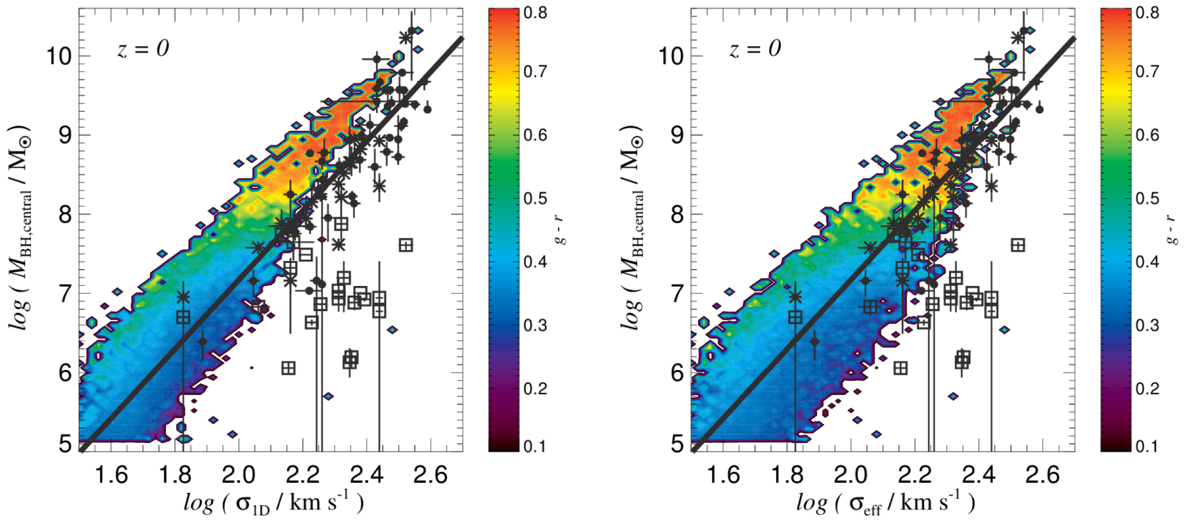

Figure 6. Black hole mass–stellar velocity dispersion relation at $z = 0$. Illustris results are shown as 2D histograms colour coded according to the host galaxies $g - r$ colours. In the left-hand panel we compute the 1D velocity dispersion of stars, $\sigma_{\rm 1D}$, from the mass-weighted 3D velocity dispersion within the stellar half-mass radius. In the right-hand panel we instead compute $\sigma_{\rm eff} = (\sigma_{\rm 1D}^2 + V_{\rm rot}^2)^{0.5}$ within the stellar half-mass radius (see text for more details). On both panels the thick black line denotes the best-fitting $M_{\rm BH}$–σ relation at $z = 0$ from Kormendy & Ho (2013) fitted to ellipticals and galaxies with bulges only. Symbols with error bars are from Kormendy & Ho (2013) as well, where circles are for ellipticals, stars are for spirals with a bulge and squares are for pseudo-bulges. Illustris agrees well with the observational findings, especially if, like for the observations, $\sigma_{\rm eff}$ is used as a proxy of stellar velocity dispersion.

$M_{\rm BH}$–$M_{\rm bulge}$ relation from $z = 0$ to 4.[6] This is in agreement with the works by Hopkins et al. (2007b) and Di Matteo et al. (2008) who also found that at fixed stellar mass black holes are more massive at higher redshifts. Note that the trend found by Di Matteo et al. (2008) is more evident for galaxies with stellar masses larger than $6 \times 10^{10}\,{\rm M}_\odot$.

We finally note that, as expected, there is a very strong trend along the simulated $M_{\rm BH}$–$M_{\rm bulge}$ relation for more massive black holes to have higher bolometric luminosities. There are, however, some very interesting further trends with cosmic time, namely: (i) for low-mass black holes bolometric luminosities are highest at early times and decrease thereafter; (ii) the same holds at the massive end where $10^9\,{\rm M}_\odot$ black holes are powering QSOs with 10^{47} erg s^{-1} luminosities preferentially at high redshifts; (iii) the engines of 10^{44} erg s^{-1} QSOs (corresponding to green colours on the histograms) systematically shift from $\sim 10^7$ to $\sim 10^9\,{\rm M}_\odot$ black holes over the redshift interval considered. These are the tell-tale signs of cosmic downsizing of the whole AGN population, which we will investigate in more detail in Sections 3.5 and 3.6.

3.4.3 $M_{\rm BH}$–σ relation at $z = 0$

In Fig. 6 we show the simulated $M_{\rm BH}$–σ relation at $z = 0$. The two panels are for two different ways to compute the velocity dispersion of the stars. In the left-hand panel we calculate mass-weighted 1D velocity dispersions of the stars, $\sigma_{\rm 1D}$, within the stellar half-mass radii with respect to the mean mass-weighted stellar velocity within the same radius where we average the full 3D velocity dispersion. In the right-hand panel we compute the rotational velocity within the stellar half-mass radius, by calculating the mass-weighted angular momentum of the stars divided by the mass-weighted mean stellar radius within the stellar half-mass radius. We then take the rms average of this rotational velocity and the previously computed $\sigma_{\rm 1D}$ which we denote as $\sigma_{\rm eff}$. Observationally velocity dispersion of the stars is typically calculated as

$$\sigma^2 = \frac{\int_{r_{\rm min}}^{r_{\rm eff}} \left(\sigma^2(r) + V_{\rm rot}^2(r)\right)\, I(r) {\rm d}r}{\int_{r_{\rm min}}^{r_{\rm eff}} I(r){\rm d}r}\,, \tag{1}$$

where $r_{\rm eff}$ is the effective radius,[7] $I(r)$ is the stellar surface brightness profile, $\sigma(r)$ is the line-of-sight velocity dispersion and $V_{\rm rot}$ is the rotational velocity (Gültekin et al. 2009; Kormendy & Ho 2013; McConnell & Ma 2013). While Gültekin et al. (2009) argue that $V_{\rm rot}$ is typically small compared to σ for a subset of their galaxies that have central stellar velocity dispersion measurement available from HyperLEDA, Harris et al. (2012) show that many of their galaxies hosting type 1 AGN exhibit a significant rotational component. For these reasons, we show the simulated $M_{\rm BH}$–σ relation both with $\sigma_{\rm 1D}$ and $\sigma_{\rm eff}$. Furthermore, we have verified that if we compute $\sigma_{\rm 1D}$ within half (or twice) the stellar half-mass radius the $M_{\rm BH}$–σ relation is essentially unchanged. Thick black lines denote the best-fitting $M_{\rm BH}$–σ relation at $z = 0$ from Kormendy & Ho (2013) fitted to ellipticals and galaxies with bulges only. Symbols with error bars are from Kormendy & Ho (2013) as well, where circles are for ellipticals, stars are for spirals with a bulge and squares are for pseudo-bulges.

From Fig. 6 we draw several important conclusions: (i) the rotational velocity is very subdominant for the galaxies hosting the most massive black holes, where $\sigma_{\rm 1D}$ and $\sigma_{\rm eff}$ give very similar results; (ii) for black hole masses less than $10^9\,{\rm M}_\odot$ a fraction of galaxies have a non-negligible $V_{\rm rot}$ component such that for a given black hole mass the stellar velocity dispersion can be shifted further

[6] Note that this best-fitting relation should not be directly compared with the best-fitting relation from Kormendy & Ho (2013) as the two fits have been performed on very different samples of galaxies.

[7] Note that in practice different authors average over a different range of radii.

Table 2. The best-fitting simulated $\log(M_{\rm BH}/{\rm M}_\odot) = A\log(\sigma/{\rm km\,s^{-1}}) + B$ relation from $z=0$ to 4, where A is the slope and B the normalization. Here we take into account only black holes hosted by galaxies with stellar half-masses greater than $10^8\,{\rm M}_\odot$, as we did for the $M_{\rm BH}$–$M_{\rm bulge}$ relation as well. Top 5 rows are for $\sigma_{\rm 1D}$, while the bottom two rows are for $\sigma_{\rm eff}$ (see text for more details).

Redshift	Slope	Normalization
For $\sigma_{\rm 1D}$		
$z=0$	5.04	−2.69
$z=1$	4.97	−2.62
$z=2$	4.81	−2.37
$z=3$	4.64	−2.16
$z=4$	4.26	−1.60
For $\sigma_{\rm eff}$		
$z=0$	4.42	−1.83
$z=1$	4.24	−1.48

to the right, increasing the scatter of the $M_{\rm BH}$–σ relation; (iii) at the massive end the agreement between the Illustris prediction and observational findings is very good, especially if we use $\sigma_{\rm eff}$ (for the best-fitting relation see Table 2), but note that at fixed black hole mass our simulated $\sigma_{\rm eff}$ is still on average slightly lower than the Kormendy & Ho (2013) sample of ellipticals; (iv) at the low-mass end the inclusion of $V_{\rm rot}$ does not help us to completely explain the scatter seen in the pseudo-bulges (even though there are a few simulated galaxies which have extremely high σ values for their black hole mass). Future observations of low σ galaxies hosting supermassive black holes will be crucial to constrain $M_{\rm BH}$–σ relation at the low black hole mass end. In terms of host galaxy colours we see the same trends described for the $M_{\rm BH}$–$M_{\rm bulge}$ relation, namely a well-defined sequence of increasingly red $g-r$ colours with higher black hole mass and over-/undermassive black holes hosted by the redder/bluer than average galaxies at a given σ.

3.4.4 Redshift evolution of the $\mathrm{M_{BH}}$–σ *relation*

We now explore the difference between $\sigma_{\rm 1D}$ and $\sigma_{\rm eff}$ at $z=1$ to identify possible systematic uncertainties for the future observational determinations of the $M_{\rm BH}$–σ relation, given that currently the vast majority of $M_{\rm BH}$–σ measurements are for $z \lesssim 1.0$ (for high-redshift measurements see e.g. Salviander & Shields 2013). As the fraction of rotationally supported systems is higher at $z=1$ than at $z=0$ we find that the inclusion of the rotational velocity becomes a more significant effect leading to a larger scatter and a different slope and normalization of the best-fitting relation, as shown in Table 2.[8] We thus conclude that the observational uncertainties and systematic biases in the $M_{\rm BH}$–σ relation at $z=0$ (see also Bellovary et al. 2014), and especially at $z>0$ could be more significant than currently assumed. At $z>0$ there are other important biases stemming from samples based on the AGN luminosity (Lauer et al. 2007) and from the uncertainty associated with the single-epoch virial black hole mass estimators (Shen & Kelly 2010), which both lead to systematic overestimation of black hole masses (see also discussion about the evolution of the $M_{\rm BH}$–$M_{\rm bulge}$ relation by Kormendy & Ho 2013). Thus, the real evolutionary trends of black hole–host galaxy relations with cosmic time are currently rather uncertain.

By comparing Figs 6 and 7 for which 2D histograms have been both colour coded according to the rest-frame $g-r$ colours we can quantify how colours of galaxies hosting supermassive black holes evolve with cosmic time. We find that for a given black hole mass, galaxies at $z=1$ are bluer. However the overall trend of a well-defined sequence of increasingly redder $g-r$ colours along the relation and over/undermassive black holes sitting in redder/bluer than average galaxies at a given σ still remains, highlighting the importance of AGN feedback for $z>0$.

In Fig. 8 we show the simulated $M_{\rm BH}$–σ relation at $z=1$, 2, 3 and 4, where we only show the result for $\sigma_{\rm 1D}$. Here the colour coding is according to the total gas mass within the stellar half-mass radius and the thick solid line is the fit from Kormendy & Ho (2013) to $z=0$ ellipticals and bulges. There are several important features to note: (i) for $z>0$ the scatter in the $M_{\rm BH}$–σ relation is larger than for the $M_{\rm BH}$–$M_{\rm bulge}$ relation even without including the effect of rotational velocity; (ii) the scatter in the relation significantly increases at higher redshifts. We have verified that calculating velocity dispersion in different ways does not decrease the scatter (e.g. computing $\sigma_{\rm 1D}$ with respect to the median velocity or the mean velocity of the whole subhalo, computing $\sigma_{\rm 1D}$ within twice of the stellar half-mass radius, defining the centre as the centre of mass of the whole subhalo or as the position of the black hole particle, changing the bin size of 2D histograms); (iii) due to the finite box size we are not able to probe the redshift evolution of black holes at the massive end, but we note that once black holes reach the $M_{\rm BH}$–σ relation they tend to stay on it (or become somewhat more massive); (iv) most of the evolution happens at the low-mass end, where a large fraction of black holes at high redshifts is below the $z=0$ relation; (v) this also drives a strong steepening of the simulated best-fitting slope with cosmic time which evolves from $\sim$4.26 at $z=4$ to $\sim$5.04 at $z=0$ (for further details see Table 2); (vi) as evident from colour coding the total gas mass within the stellar half-mass radius not only increases with σ (which would be a simple dependence on host halo mass), but it also shows a trend roughly perpendicular to the best-fitting relation: for a given σ undermassive black holes live in more gas-rich environments than is the case for the overmassive black holes and this difference is up to a factor of 10. This demonstrates that the strong AGN feedback not only quenches galaxy colours but it also efficiently expels gas from the galaxies' innermost regions.

The evolution of the slope of the simulated $M_{\rm BH}$–σ relation is very interesting. According to the well-established analytical models (Haehnelt et al. 1998; Silk & Rees 1998; Fabian & Iwasawa 1999; King 2003) and as recently demonstrated by detailed numerical simulations (Costa et al. 2014a) momentum-driven AGN outflows lead to a slope of the $M_{\rm BH}$–σ relation equal to 4, whereas energy-driven outflows correspond to steeper slopes of 5. While we are not directly injecting any momentum into the medium surrounding black holes, large energy injections where the gas becomes outflowing and where at the same time considerable energy is lost due to the radiation resemble momentum-driven flows and lead to slopes of the $M_{\rm BH}$–σ relation closer to 4. Conversely, large energy injections where most of the energy is not radiated away should lead to slopes closer to 5. The evolutionary trend that we see in Illustris can thus be interpreted in the following way: at high redshifts there are copious amounts of very dense and cold gas due to the rapid

[8] It is interesting to note that Kassin et al. (2007) also consider the combination of the rotational velocity and velocity dispersion of the gas when studying the redshift evolution of the stellar mass Tully–Fisher relation, but find that the scatter is reduced with respect to using gas rotational velocity alone.

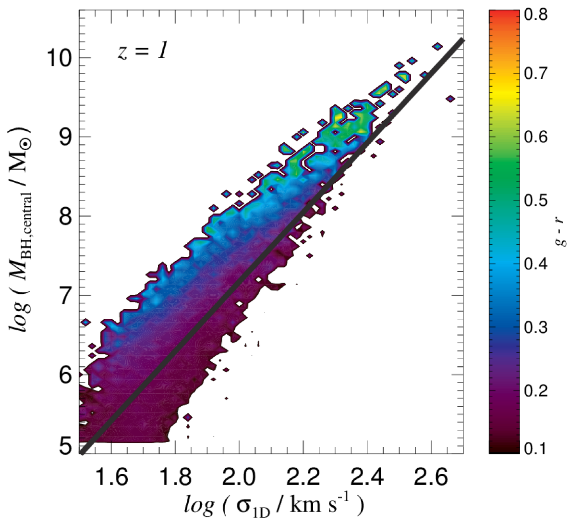

Figure 7. Black hole mass–stellar velocity dispersion relation at $z = 1$. Illustris results are shown as 2D histograms colour coded according to the host galaxies $g - r$ colours (rest frame). In the left-hand panel we compute the 1D velocity dispersion of stars, $\sigma_{\rm 1D}$, from the mass-weighted 3D velocity dispersion within the stellar half-mass radius. In the right-hand panel we instead compute $\sigma_{\rm eff} = (\sigma_{\rm 1D}^2 + V_{\rm rot}^2)^{0.5}$ within the stellar half-mass radius (see text for more details). On both panels the thick black line denotes the best-fitting $M_{\rm BH}$–σ relation at $z = 0$ from Kormendy & Ho (2013) fitted to ellipticals and galaxies with bulges only. Note the considerable evolution in host galaxy colours from $z = 0$ (see Fig. 6), and that the rotational velocity is now contributing more to $\sigma_{\rm eff}$ at almost all black hole masses.

cooling regime (White & Frenk 1991; Birnboim & Dekel 2003; Nelson et al. 2013) and thus AGN-injected energy can be easily radiated away, leading to a $M_{\rm BH}$–σ relation with a slope of ∼4; at low redshifts and especially in massive galaxies there is less cold gas inflow as gas is supported by quasi-hydrostatic atmospheres. Thus AGN feedback becomes more energy driven. This is particularly the case for our 'radio' mode heating which is more bursty, more energetic and thus less prone to the radiative losses. Moreover, at lower redshifts, $z \lesssim 2$, AGN feedback starts to become very efficient at quenching galaxies and more dry mergers take place. Dry mergers tend to increase both black hole and stellar mass, while keeping the stellar velocity dispersion largely unchanged (see e.g. Boylan-Kolchin, Ma & Quataert 2006). Taken together, these arguments may help explain why the slope of the $M_{\rm BH}$–σ steepens for the most massive black holes, as seen in observations.

3.5 Eddington ratios

In Fig. 9 we show the distribution of black hole Eddington ratios from $z = 4$ to 0 (left-hand panel) and the mean and median Eddington ratios as a function of black hole mass for the same redshift interval (right-hand panel). Note that for Eddington ratios lower than $\lambda_{\rm Edd} = 10^{-4}$ (denoted with a dashed vertical line) the model is not well converged. While the distribution of Eddington ratios is quite broad there is a clear trend with cosmic time (see also e.g. Sijacki et al. 2007; Di Matteo et al. 2008). At high redshifts the majority of black holes accrete at a high rate and the mean Eddington ratio is essentially flat as a function of black hole mass. With cosmic time the peak of the Eddington ratio distribution systematically shifts towards lower $\lambda_{\rm Edd}$ values, the fraction of the population accreting at the maximal rate decreases, while at the same time a larger tail of very low Eddington accretors builds up. Mean Eddington ratios at $z = 0$, 1, 2, 3 and 4 are $\langle \log \lambda_{\rm Edd} \rangle = -3.6, -2.6, -1.8, -1.2$ and -0.7, while if we consider only AGN with bolometric luminosities greater than 10^{42} erg s^{-1} the respective values are -2.3, -1.6, -1.2, -0.8 and -0.5. These results are in good qualitative agreement with a study of broad-line SDSS quasars by Shen & Kelly (2012), whose mean Eddington ratios interpolated on the same redshifts yield -2.2, -1.5, -1.0, -0.7 and -0.4. Interestingly, while Shen & Kelly (2012) find a strong evolution of the mean Eddington ratio with redshift, they do not find that it strongly depends on the black hole mass, similar to our simulation results. Note, however, that the comparison with Shen & Kelly (2012) is not straightforward as our sample is volume limited and theirs is flux limited. At the massive end, i.e. $\geq 2 \times 10^9$ M$_\odot$, the mean $\lambda_{\rm Edd}$ drops most with decreasing redshift, which is a clear signature of cosmic downsizing. We will explore this further in Section 3.6 where we will directly link our simulation results with the observational findings.

In Fig. 10 we explore how the distribution of $g - r$ colours (left-hand panel) and stellar masses within half-mass radii (right-hand panel) of galaxies at $z = 0$ depends on the Eddington ratios of their central black holes. The black dashed histogram denotes the median of the distribution, and shaded region encloses the 5th–95th percentile of the distribution. The coloured histograms are for galaxies hosting black holes in different mass ranges, as specified in the caption. For any given $\lambda_{\rm Edd}$ there is a very large spread in galaxy colours and stellar masses. The median of the distributions is driven by galaxies hosting low-mass black holes, as can be seen by comparing the black dashed and blue histograms. However, we find that black holes more massive than 10^8 M$_\odot$ live in redder and more massive galaxies but have a vast range of Eddington ratios (consistent with the findings from Fig. 9). Only for the highest $\lambda_{\rm Edd}$ values, i.e. greater than 0.1, the distribution of $g - r$ colours narrows, corresponding to galaxies that have black holes just below the $M_{\rm BH}$–$M_{\rm bulge}$ and $M_{\rm BH}$–σ relations.

We further investigate which population of galaxies and black holes is responsible for the two distinct peaks seen in the distribution of $g - r$ colours. We find that the peak with $\lambda_{\rm Edd} < -5.7$ and $g - r > 0.55$ corresponds to a distinct population which lies at the tip of the massive end of the simulated $M_{\rm BH}$–$M_{\rm bulge}$ relation. These galaxies also have low specific star formation rates and on average low gas content (even though there is a considerable scatter). The second peak, i.e. $-3.2 < \lambda_{\rm Edd} < -1.2$ and $g - r > 0.55$, is instead caused by galaxies with a mix of properties, which can be

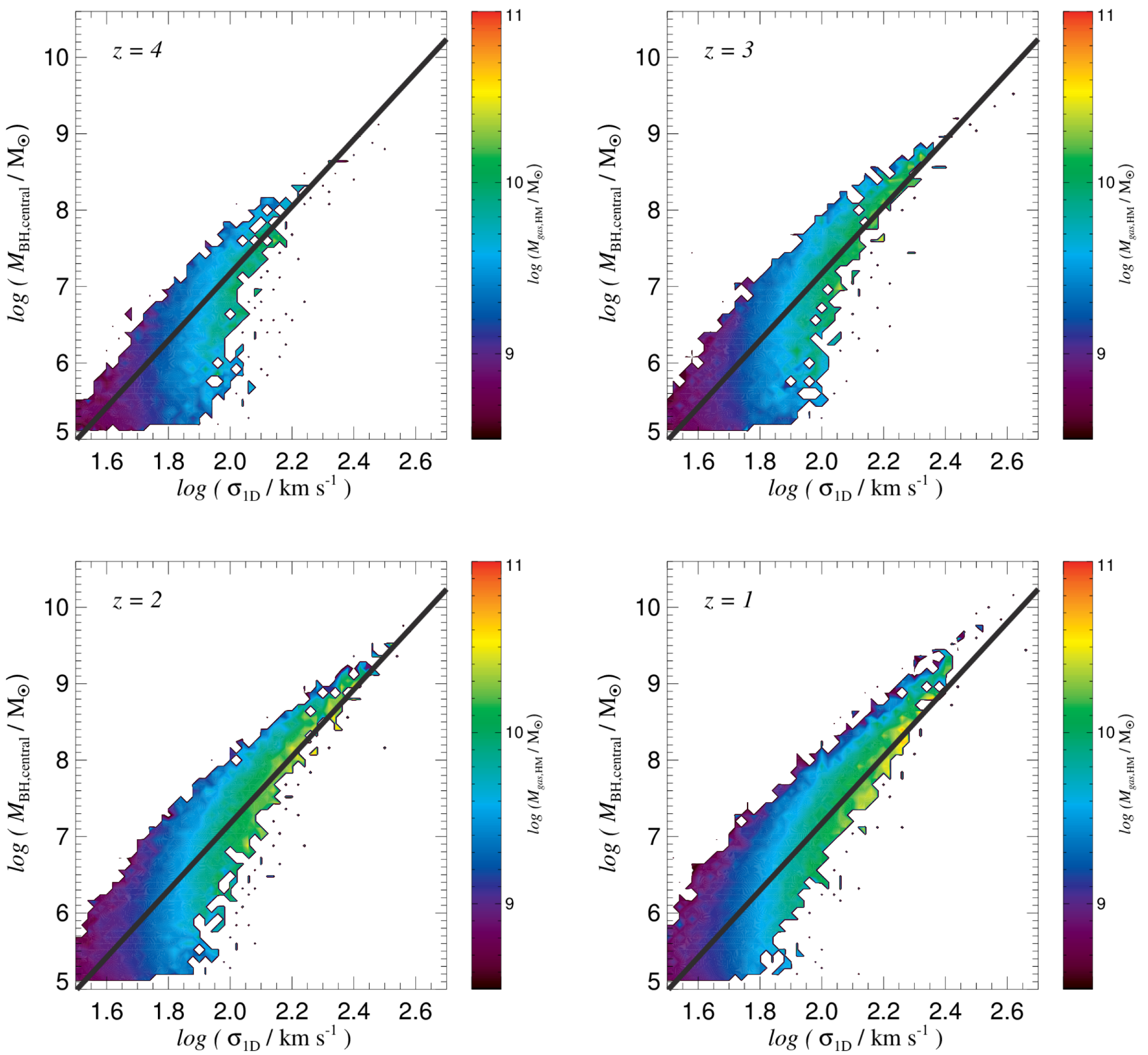

Figure 8. Redshift evolution of the black hole mass–stellar velocity dispersion relation at $z = 4$, 3, 2 and 1. Illustris results are shown as 2D histograms, where colour coding is according to the total gas mass within stellar half-mass radius. The thick solid line is the fit from Kormendy & Ho (2013) to $z = 0$ ellipticals and bulges, as in Fig. 6. Simulation results indicate that the $M_{\rm BH}$–σ relation is evolving with the slope steepening from ~4.26 at $z = 4$ to ~4.97 at $z = 1$.

roughly divided into three categories: (i) a large fraction of galaxies are occupying the massive end of the $M_{\rm BH}$–$M_{\rm bulge}$ relation, but on average they have somewhat smaller black hole masses than is the case for galaxies with $\lambda_{\rm Edd} < -5.7$ and $g - r > 0.55$. They also typically have low specific star formation rates, but are on average more gas rich (again with a very large scatter); (ii) the second category consists of galaxies with a very wide range of black hole masses, but at a given $M_{\rm bulge}$ all of these black holes lie above the best-fitting relation; due to the 'overmassive' black holes the host galaxies have low specific star formation and gas mass fraction; (iii) finally, the third category consists of galaxies with low-mass black holes whose feedback is not strong enough to affect their hosts. Here, instead, outflows from supernova-driven winds lead to red galaxy colours, low specific star formation rates and low gas masses.

3.6 AGN luminosity functions

In Fig. 11 we compare the AGN bolometric and hard X-ray luminosity functions as predicted by the Illustris simulation at $z = 0$, 1, 2 and 3 with observations. We refrain from comparing against the soft X-ray or *B*-band luminosity functions because of large uncertainties in the obscuration fractions and host galaxy contamination which could significantly bias the interpretation of the results. Note however that even in the case of the bolometric and hard X-ray luminosity functions large uncertainties remain due to poorly constrained bolometric corrections (Hopkins et al. 2007a; Vasudevan & Fabian 2007, 2009; Lusso et al. 2012) and the uncertain fraction of Compton-thick sources for $z \gtrsim 0$ (e.g. see recent papers by Ueda et al. 2014; Aird et al. 2015; Buchner et al. 2015).

Keeping these caveats in mind, we compare the Illustris AGN bolometric luminosity function with the bolometric luminosity function as derived by Hopkins et al. (2007a), which is still the standard reference in the field. When computing the bolometric luminosity function we do not consider black holes with Eddington ratios smaller than 10^{-4}, which is a very conservative estimate given that these objects should be in a radiatively inefficient regime. For the hard X-ray luminosity function we compute the simulated X-ray luminosities from our bolometric luminosities by adopting the bolometric corrections of Hopkins et al. (2007a). We have also

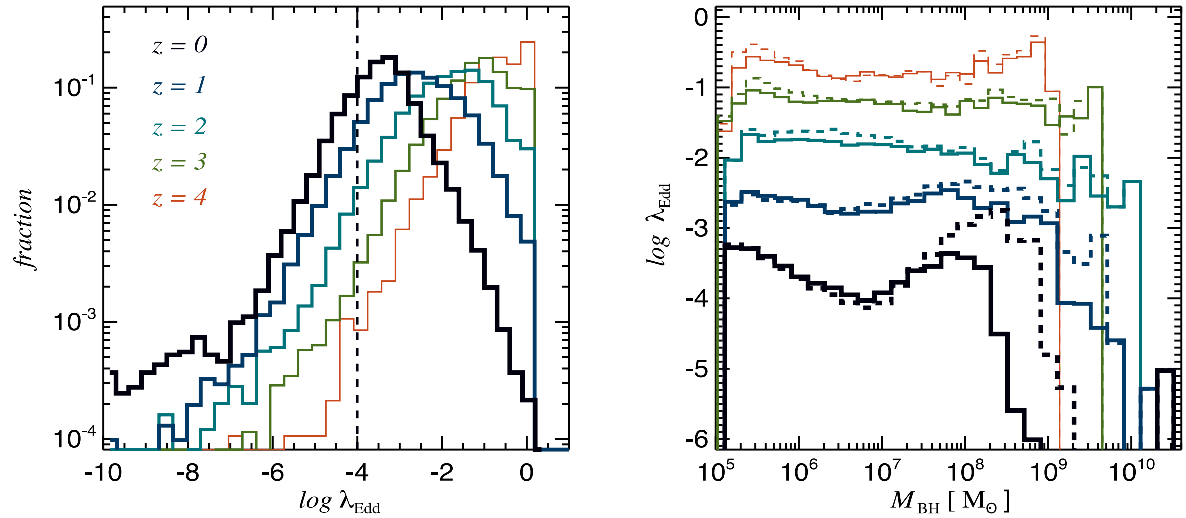

Figure 9. Left: distribution of black hole Eddington ratios at $z = 4$, 3, 2, 1 and 0, as indicated on the legend. For Eddington ratios lower than $\lambda_{\rm Edd} = 10^{-4}$ (dashed vertical line) the model is not well converged. There is a clear evolution in the Eddington ratios with cosmic time, with many black holes accreting close to the maximal rate at $z = 4$, while for $z = 0$ the mean Eddington ratio is low. Right: Eddington ratios as a function of black hole mass at $z = 4$, 3, 2, 1 and 0 (same colour coding as on the left-hand panel). Continuous lines denote the mean of the logarithm of $\lambda_{\rm Edd}$ in each bin, while the dashed lines show the median values. Apart from $z = 0$ result where the average Eddington ratio is lowest for $\sim 10^7\,{\rm M}_{\odot}$ black holes, the distribution of $\lambda_{\rm Edd}$ is fairly flat. Note that at the massive end, i.e. $M_{\rm BH} \geq 2 \times 10^9\,{\rm M}_{\odot}$, the mean $\lambda_{\rm Edd}$ drops most with decreasing redshift, which is a clear signature of cosmic downsizing.

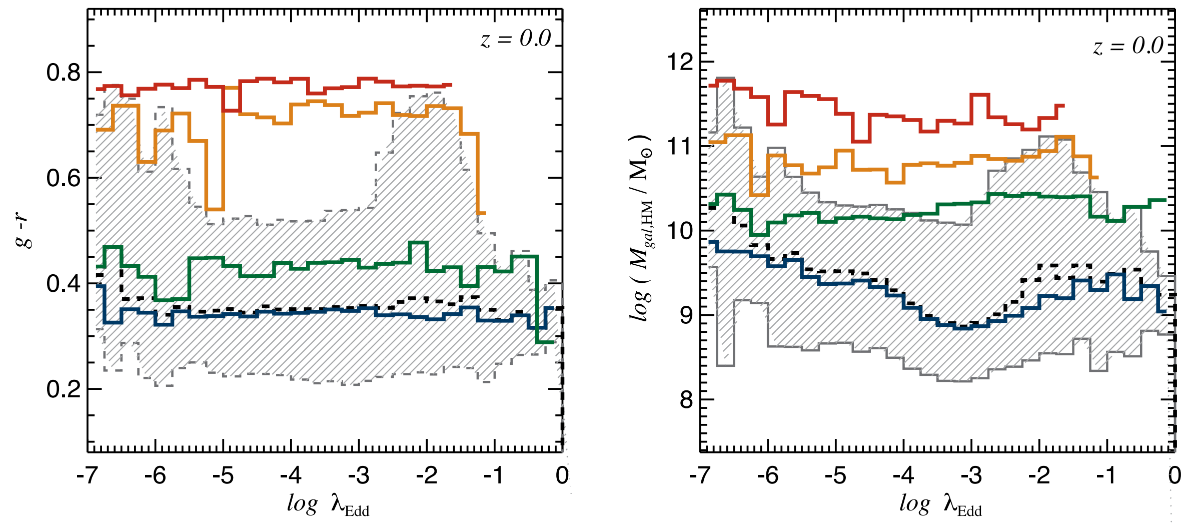

Figure 10. Distribution of $g - r$ colours (left) and stellar masses within the half-mass radii (right) of galaxies at $z = 0$ as a function of the Eddington ratios of their central black holes. The black dashed histogram denotes the median of the distribution, and the shaded region encloses the 5th–95th percentile of the distribution. Coloured histograms are for galaxies hosting black holes in different mass ranges: $M_{\rm BH} < 10^7\,{\rm M}_{\odot}$ (blue), $10^7 \leq M_{\rm BH} < 10^8\,{\rm M}_{\odot}$ (green), $10^8 \leq M_{\rm BH} < 10^9\,{\rm M}_{\odot}$ (orange), $10^9\,{\rm M}_{\odot} \leq M_{\rm BH}$ (red), where the colours have been chosen to roughly match the colour coding of Fig. 4. For any given $\lambda_{\rm Edd}$ there is a very large spread in galaxy colours and stellar masses, while the median of the distributions is driven by galaxies hosting low-mass black holes. More massive black holes live in redder and more massive galaxies but have a vast range of Eddington ratios, with a clear trend only for the highest $\lambda_{\rm Edd}$ values.

corrected the hard X-ray luminosities assuming the obscuration fraction given by equation (4) in Hopkins et al. (2007a) which is redshift independent.

We compare our hard X-ray luminosity function with the most recent compilation by Ueda et al. (2014). By assuming bolometric corrections from Hopkins et al. (2007a) as well, Ueda et al. (2014) showed that to reconcile the black hole mass function obtained from the revised $M_{\rm BH}$–$M_{\rm bulge}$ relation (Kormendy & Ho 2013) with the black hole mass function calculated from the bolometric luminosity function using Soltan-type arguments, the mean radiative efficiencies of AGN need to be revised downwards. Assuming an average Eddington ratio of ∼0.7 that does not depend on redshift or AGN luminosity, Ueda et al. (2014) determine a mean radiative efficiency of $\epsilon_{\rm r} \sim 0.05$.

We start our analysis by fixing the radiative efficiency to 0.05 as shown in Fig. 11. This is not the value that yields the best match to the observed luminosity functions, but it is merely motivated by the considerations made by Ueda et al. (2014). Note that any constant value of $\epsilon_{\rm r}$ simply changes the normalization but not the shape of the luminosity functions. For $\epsilon_{\rm r} = 0.05$ we find good agreement with observations at all redshifts, both for bolometric and hard X-ray luminosity functions, at the bright end. For $z \geq 2$

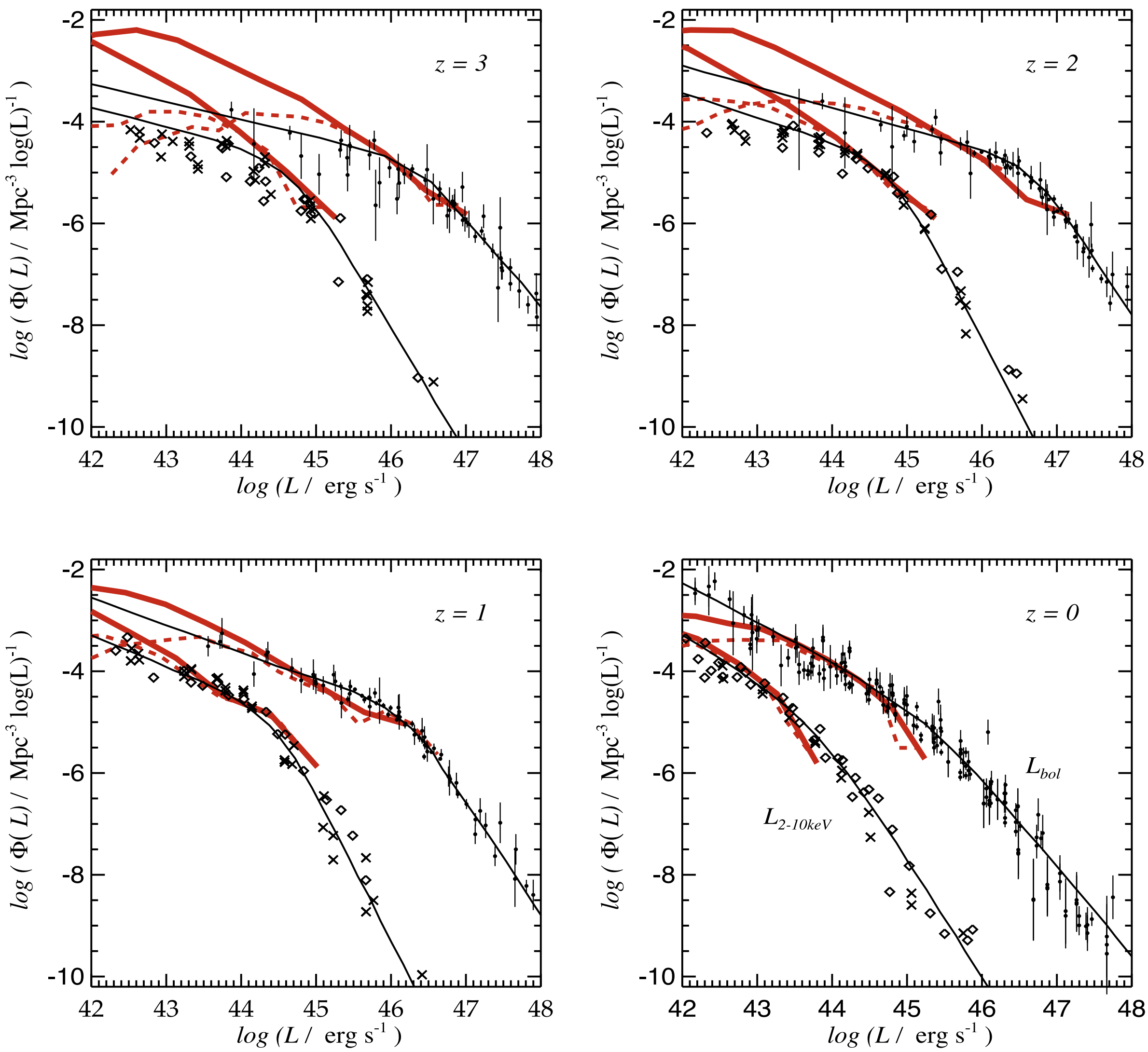

Figure 11. AGN bolometric and hard X-ray luminosity functions at $z = 0$, 1, 2 and 3. Illustris results are shown with thick red lines. A constant radiative efficiency of 0.05 is assumed and black holes with Eddington ratio greater than 10^{-4} are plotted. Dashed red lines denote results for black holes that are additionally more massive than $5 \times 10^7\,M_{\odot}$. For bolometric luminosity functions data points with error bars are from the compilation by Hopkins, Richards & Hernquist (2007a), while for hard X-ray luminosity functions additional data points are taken from Ueda et al. (2014). Thin black lines are best-fitting evolving double power-law models to all redshifts from Hopkins et al. (2007a) (see their figs 6 and 7). Overall we find good agreement with the observed AGN luminosity functions at the bright end, while for $z > 1$ we overpredict the number of faint AGN, unless low-mass black holes are excluded.

we overpredict the number of faint AGN with $L_{\rm bol} < 10^{45}\,{\rm erg\,s^{-1}}$ and $L_{\rm 2-10\,keV} < 10^{44}\,{\rm erg\,s^{-1}}$. However, if we consider only black holes more massive than $5 \times 10^7\,M_{\odot}$ (dashed red lines) we can obtain a better agreement both in the case of the bolometric and hard X-ray luminosity function at the faint end, while the bright end remains essentially unchanged.

There are several important conclusions to draw from this comparison: (i) for our simulated Eddington ratios, constant $\epsilon_{\rm r}$ values of $\geq$0.1 are inconsistent with the data. This is in agreement with the conclusions by Ueda et al. (2014) even though they assume a very different $\lambda_{\rm EDD}$. Comparison with data at higher redshifts, i.e. $z \geq 1$, is particularly constraining given that the majority of our simulated AGN are in the radiatively efficient regime at these epochs; (ii) a low constant value of $\epsilon_{\rm r} = 0.05$ implies that our feedback efficiency should be 0.2 instead of 0.05 (given that the product of these is degenerate, see Section 2.4.2) if we are to successfully reproduce black hole mass function and black hole–galaxy scaling relations; (iii) there are several lines of both theoretical and observational evidence (e.g. Mahadevan 1997; Ciotti, Ostriker & Proga 2009; Ueda et al. 2014) indicating that radiative efficiencies might depend on black hole properties, such as their accretion rate. By setting $\epsilon_{\rm r} = 0.1$ for all black holes in the 'quasar' mode and by computing an accretion-rate-dependent $\epsilon_{\rm r}$ for black holes in the 'radio' mode (following Mahadevan 1997; Ciotti et al. 2009) we can also get a good match to the observed luminosity functions at $z = 0$. Thus, even though we cannot uniquely constrain radiative efficiencies, on average they should still be low. Alternatively, radiative efficiencies could be higher if the bolometric corrections are currently largely underestimated. This is a very interesting prediction of our model that can be verified once robust estimates of Eddington ratios for a range of black hole masses and redshifts become available, which would break the degeneracies between Eddington ratio and radiative efficiency distributions.

We now discuss the possible systematic biases at the faint end of the AGN luminosity function for $z \gtrsim 1$. Given that the X-ray luminosity function determined by Ueda et al. (2014) is de-absorbed we would not need to apply any obscuration correction, except for the contribution from Compton-thick sources which is uncertain (see also a recent paper by Aird et al. 2015, which agrees with Ueda et al. 2014 findings). However, the Ueda et al. (2014) sample is flux limited, while our sample is volume limited. In fact our number density of AGN is dominated by low-luminosity objects while Ueda et al. (2014) find only around 40 sources for $z > 2$ with $L_{2-10\,\mathrm{keV}} \le 10^{43}\,\mathrm{erg\,s^{-1}}$. Thus, some fraction of the discrepancy at the faint end between our X-ray luminosity function and the observational one could be due to this mismatch. There are other important sources of uncertainties as well. Radiative efficiencies could be luminosity dependent, there could be significant biases due to the uncertainties in bolometric corrections, or the Illustris predictions could be wrong. In particular, with regard to this last possibility, if we compute luminosity functions for black holes more massive than $5 \times 10^7\,\mathrm{M_\odot}$ the agreement with both bolometric and hard X-ray luminosity function is greatly improved. This suggests that part of the discrepancy could be attributed to our seeding prescription and to the accretion on to low-mass black holes which is not well converged and where black holes have not yet reached the self-regulated regime. This also affects our simulated black hole mass function at the low-mass end as we have discussed in Section 3.3. Finally, it is interesting to note that a recent paper by Buchner et al. (2015) advocates significantly larger uncertainties at the faint-end of the AGN luminosity function which stem from their non-parametric approach. Future observations of the faint end of the AGN luminosity function and robust determination of the fraction of Compton-thick sources as a function of redshift will be crucial to shed light on these issues.

Keeping these uncertainties in mind, in Fig. 12 we now compare the redshift evolution of the comoving number density of AGN split into three bins based on their bolometric (left-hand panel) and hard X-ray luminosity (right-hand panel) with the estimates by Hopkins et al. (2007a) and Ueda et al. (2014). This is a more direct way of probing the observed cosmic downsizing of the AGN population that we have discussed in Section 3.5 in terms of Eddington ratios. We find that the Illustris simulation qualitatively reproduces observations, with the agreement being best for the highest luminosity bin and poorest for the lowest luminosity bin, both in the case of bolometric and hard X-ray luminosities. The drop of the AGN comoving number density in Illustris for $z < 2$ is systematically steeper for higher luminosity objects in agreement with observations but we do not find that the number density of lower luminosity AGN peaks at lower redshifts. Considering only black holes more massive than $5 \times 10^7\,\mathrm{M_\odot}$ (filled stars) significantly improves the agreement with data, again indicating that the modelling of low-mass black holes may have to be improved.

3.7 The link between star formation and AGN triggering

In Fig. 13 we show star formation rates within stellar half-mass radius (top panels) and stellar mass within the same radius (bottom panels) as a function of the hard X-ray luminosity of the central AGN (taking into account black holes with $\lambda_{\mathrm{Edd}} > 10^{-4}$). We compare the Illustris results with the recent study by Azadi et al. (2015) based on the Prism Multi-object Survey (PRIMUS; green diamonds) and with the COSMOS data compilation (Lusso et al. 2010, 2011, with stellar masses and star formation rates from Bongiorno et al. 2012 and redshifts from Brusa et al. 2010; red circles). The three panels are for different redshift intervals probed by the surveys while we plot the Illustris data at the mean redshift of each redshift bin. This comparison reveals why it has been so hard for the present observations to establish a clear link between star formation and AGN activity. For example, Mullaney et al. (2012) and Rosario et al. (2012) using a combination of far-infrared and X-ray data found no correlation between star formation rates and AGN X-ray luminosities, suggesting that they might be triggered by different physical processes. However, the most luminous AGN seem to be correlated with high star formation rates (see e.g. Lutz et al. 2008; Rosario et al. 2012) and Hickox et al. (2014) discussed the possibility that while star formation and black hole activity are correlated over long time-scales, AGN variability introduces a significant scatter (see also discussion in Alexander & Hickox 2012; Azadi et al. 2015).

Regardless of the redshift considered, Fig. 13 shows that there is considerable scatter in the simulated relations, such that for a given $L_{2-10\,\mathrm{keV}}$ star formation rates and stellar masses can vary by up to two orders of magnitude. For a given star formation rate the variation in $L_{2-10\,\mathrm{keV}}$ is even larger, spanning up to the full X-ray luminosity range. This demonstrates that triggering of star formation and central AGN are not necessarily always tightly linked either in terms of common origin or in terms of coherent timing. For example, minor wet mergers, cold gas inflows and local gas compression might trigger star formation but the fresh gas supply might not get funnelled to the centralmost region where the AGN resides (either due to gas consumption and/or expulsion along the way or due to the residual gas angular momentum). Moreover the timing of star formation versus AGN triggering can be different even in the case of gas-rich major mergers which do bring copious amounts of gas to the centre, as repeatedly shown in numerical simulations of isolated galaxy mergers (e.g. Springel, Di Matteo & Hernquist 2005; Sijacki, Springel & Haehnelt 2011; Thacker et al. 2014). Thus, given the large intrinsic scatter in the SFR–$L_{2-10\,\mathrm{keV}}$ plane as predicted by the Illustris simulation and given that both PRIMUS and COSMOS data cover a relatively narrow range of X-ray luminosities no correlation between the two can be observationally inferred. Note however that regardless of the large scatter there is a correlation between star formation rates and AGN luminosities in Illustris, as shown by the thick black line in Fig. 13 which is the best-fitting relation. This is to be expected as the shape of the cosmic star formation rate density is similar to the shape of the black hole accretion rate density (see Figs 1 and 2). This highlights that there is an underlying strong physical connection between star formation and black hole growth driven by large-scale cosmological gas inflows and mergers but the details of each trigger effect may vary. We furthermore explore whether some of the scatter seen in Fig. 13 is due to the AGN variability which occurs on much shorter time-scale than the changes in the star formation rate. To test this idea, similarly to the recent study by Hickox et al. (2014), we consider the $L_{2-10\,\mathrm{keV}}$–SFR plane (essentially swapping the axis with respect to Fig. 13). The best-fitting relation exhibits a slightly smaller unreduced χ^2 value, which indicates that the AGN variability contributes to the scatter seen in Fig. 13. We furthermore compute the mean $L_{2-10\,\mathrm{keV}}$ in SFR bins at $z = 0.35$, 0.65 and 1 and find an essentially redshift-independent correlation. However, the mean SFR computed in bins of $L_{2-10\,\mathrm{keV}}$ does change with redshift. Even though we probe somewhat smaller luminosities than Hickox et al. (2014) this is in qualitative agreement with their findings (see also Azadi et al. 2015), further corroborating the idea that also due

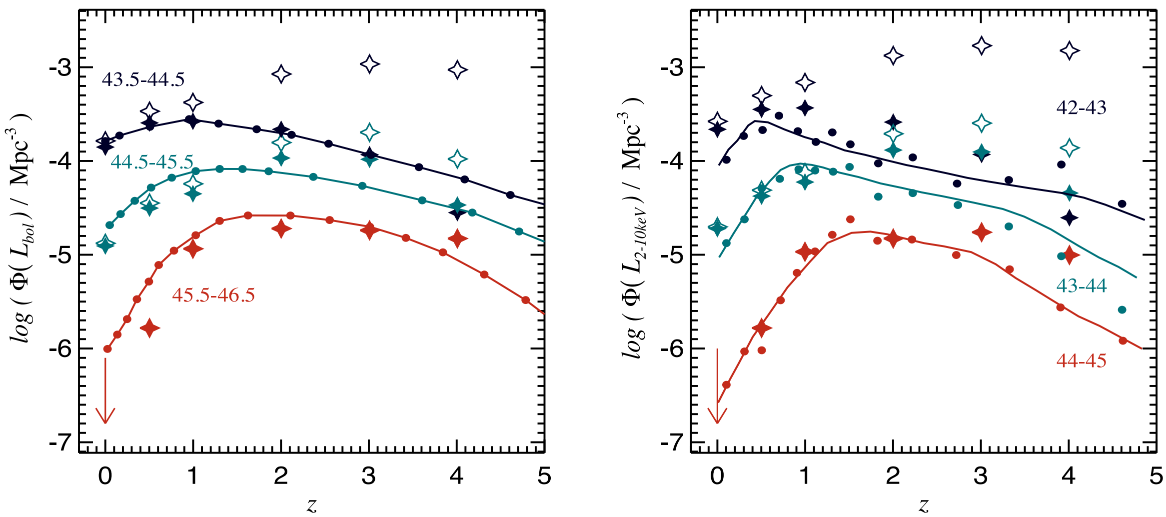

Figure 12. Left: redshift evolution of the comoving number density of AGN split into three bins based on their bolometric luminosity (in logarithmic units): 43.5–44.5 (dark blue, top curve), 44.5–45.5 (turquoise, middle curve) and 45.5–46.5 (red, bottom curve). Observational constraints from Hopkins et al. (2007a) are shown with circles joined by continuous lines, while the Illustris results are denoted with star symbols. Here we are showing the results only for black holes with Eddington ratios greater than 10^{-4} (open stars) and for black holes which are additionally more massive than $5 \times 10^7\,\mathrm{M}_\odot$ (filled stars). A constant radiative efficiency of 0.05 is assumed. Right: redshift evolution of the comoving number density of AGN split into three bins based on their hard X-ray luminosity (in logarithmic units): 42–43 (dark blue, top curve), 43–44 (turquoise, middle curve) and 44–45 (red, bottom curve). Observational constraints from Ueda et al. (2014) are shown with circles and the continuous curves with matching colours are their best-fitting model. The Illustris results are denoted with open and filled star symbols, with the same selection criteria as in the left-hand panel.

to the underlying short-time-scale AGN variability star formation and AGN activity do not appear correlated, while in fact there is time-averaged correlation.

4 DISCUSSION AND CONCLUSIONS

In this work we have presented an overview of the main properties of black holes as predicted by the Illustris simulation. Owing to its large volume and high dynamic range we can study the properties of a representative sample of black holes embedded within host galaxies with resolved inner structural properties. The Illustris simulation volume is too small to follow the formation and evolution of the most massive black holes observed in the Universe, but it is sufficiently large that we can characterize e.g. the black hole mass function, black hole–host galaxy scaling relations and AGN luminosity functions over the most important ranges. We note that while the free parameters of the black hole model have been tuned to reproduce star formation rate history and stellar mass function at $z = 0$ (Vogelsberger et al. 2013; Torrey et al. 2014) and the quasar feedback efficiency has been selected following Di Matteo et al. (2005) and Springel et al. (2005), the main properties of black holes are a genuine prediction of our model. Thus we find it highly encouraging that the Illustris simulations reproduce several key observables, also allowing us to highlight possible biases in current data sets and to make predictions for future observational programmes. However, the successes of the model need to be considered in view of several caveats: the black hole properties are not well converged, even though the convergence properties are better for more massive black holes with Eddington ratios greater than 10^{-4} (see Appendix); our seeding prescription is rather simplistic and uncertain, as detailed in Section 3.3, which also leads to a likely overprediction of the black hole merger rates; unavoidably, due to resolution limitations, accretion on to low-mass black holes is not well resolved. Keeping these caveats in mind our main findings are as follows.

(i) We find that the black hole mass density over the whole redshift range probed by observations, i.e. for $z < 5$, is consistent with the estimate based on the most up-to-date hard X-ray survey compilation by Ueda et al. (2014). For black holes more massive than $10^7\,\mathrm{M}_\odot$ the mass function at $z = 0$ is in good agreement with the constraints by Shankar (2013), which are based on the revised M_{BH}–σ scaling relation of McConnell & Ma (2013). These two results taken together indicate that overall we have a realistic population of black holes formed in the Illustris simulation both in terms of the total number density and also in terms of the mass distribution. However, we highlight that we overpredict the number of low-mass black holes, i.e. $M_{\mathrm{BH}} \lesssim 10^7\,\mathrm{M}_\odot$ with respect to the estimates by Shankar (2013), which indicates that our seeding prescription is likely overproducing these objects. The accretion on to these low-mass black holes is also least well resolved in Illustris which may contribute to the discrepancy, if simulated low-mass black holes accrete too much gas.

(ii) The Illustris data set allowed us not only to construct the M_{BH}–M_{bulge} and M_{BH}–σ scaling relations which are in very good agreement with the most recent estimates (Kormendy & Ho 2013; McConnell & Ma 2013) but also to relate galaxy properties, in terms of their morphologies and colours, to the position on these relations. This permits us, for the first time to our knowledge, to pin down for which galaxy types co-evolution with their central black holes is driven by a physical link, rather than arising as a statistical by-product.

(iii) Specifically, we find that observed pseudo-bulges coincide with blue star-forming Illustris galaxies having undermassive black holes which do not significantly affect either their colours or their gas content. While some of the black hole and stellar mass assembly in these objects has a common origin, the feedback loop is not fully

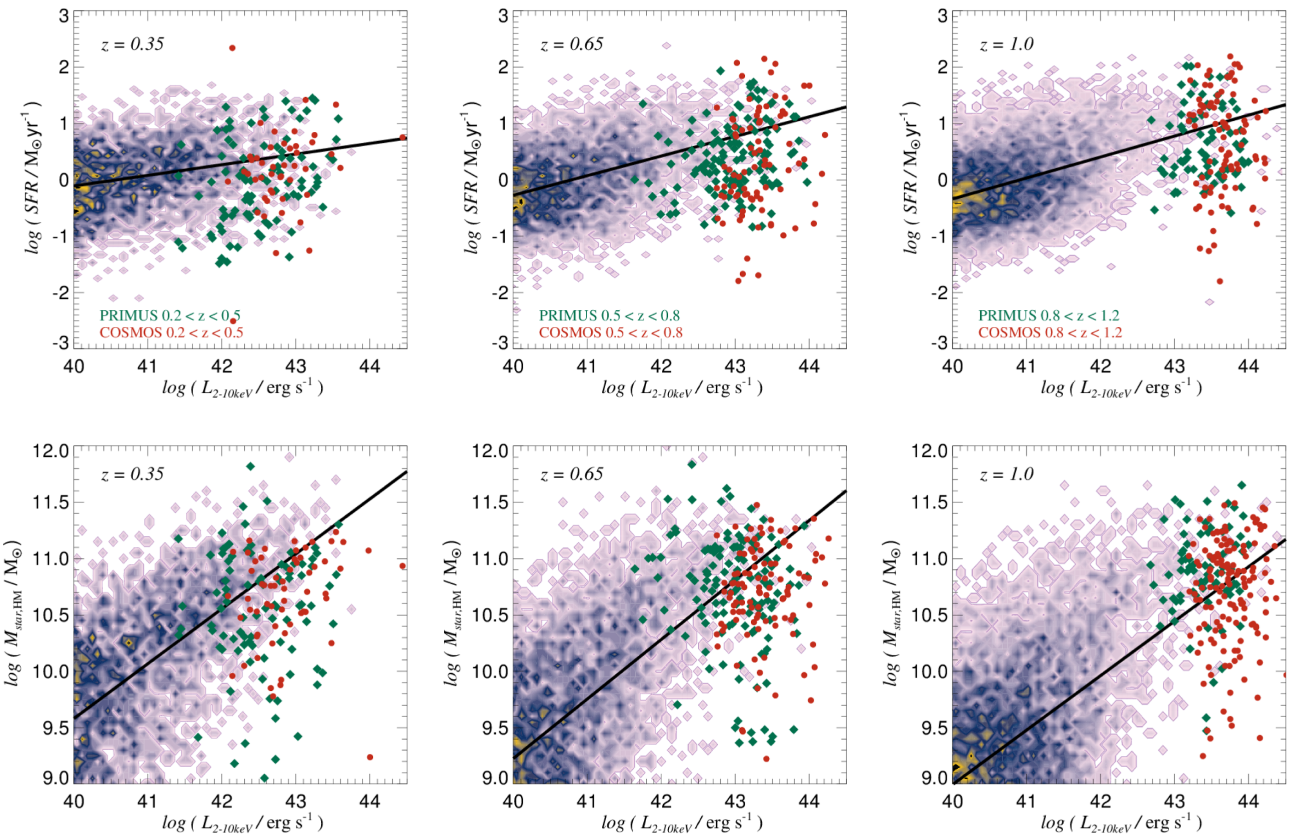

Figure 13. Top panels: star formation rate within stellar half-mass radius as a function of the hard X-ray luminosity of the central AGN. Illustris results at $z = 1$, 0.65 and 0.35 are shown with 2D histograms (colours indicate number density), while the data points (green diamonds) are for the PRIMUS galaxies from Azadi et al. (2015) and COSMOS galaxy compilation (red circles) from Lusso et al. (2010, 2011), Brusa et al. (2010) and Bongiorno et al. (2012) for the redshift ranges $0.2 < z < 0.5$, $0.5 < z < 0.8$ and $0.8 < z < 1.2$, respectively. Bottom panels: stellar mass within the stellar half-mass radius versus the hard X-ray luminosity of the central AGN for the Illustris galaxies (2D histograms), PRIMUS galaxies from Azadi et al. (2015) (green diamonds) and COSMOS galaxies (red circles). In all panels the best-fitting relation (least-square linear fit) to the Illustris galaxies is shown with a thick black line. While we do see a correlation in the simulated relations, there is a considerable scatter, such that for a given $L_{2-10\,\mathrm{keV}}$ value star formation rates and stellar masses can vary by up to two orders of magnitude.

established, and other physical processes, such as supernova-driven winds may be prevailing. This explains why at the low-mass end the scatter in the observed $M_{\rm BH}$–$M_{\rm bulge}$ and $M_{\rm BH}$–σ increases.

(iv) Interestingly, the most efficient accretors at $z = 0$ typically correspond to black holes just under the observed $M_{\rm BH}$–$M_{\rm bulge}$ relation indicating that these objects, due to a sufficient gas supply, can transform galaxy properties from blue star forming to red and quenched on short time-scales. In fact, $10^8\,{\rm M}_{\odot}$ black holes have the highest Eddington ratios on average and reside within galaxies with colours $g - r \sim 0.5$ and with a mix of morphologies, resembling the so-called 'green valley' objects (Schawinski et al. 2014).

(v) Black holes that are above the best-fitting $M_{\rm BH}$–$M_{\rm bulge}$ and $M_{\rm BH}$–σ relations or reside at the massive end are hosted by galaxies which have red colours, low gas fractions and low specific star formation rates. This directly demonstrates that for these systems there is a strong physical link between galaxy properties and their central black holes and co-evolution does take place.

(vi) By examining the redshift evolution of the $M_{\rm BH}$–$M_{\rm bulge}$ and $M_{\rm BH}$–σ relations, we find that black hole growth precedes galaxy assembly, where for a given bulge mass black holes for $z > 0$ are more massive than their $z = 0$ counterparts. This is also in line with the shape of the black hole accretion rate density which rises more steeply than the cosmic star formation rate density for $z > 2$. The redshift evolution of the slope of the $M_{\rm BH}$–σ relation indicates that at high redshifts there are significant radiative losses in the AGN-driven outflows while at low z and especially in massive objects radiation losses are subdominant so that the energy-driven flow is established. Additionally, at low redshifts more dry mergers take place, as AGN feedback becomes more efficient at quenching galaxies, which has been shown (see e.g. Boylan-Kolchin et al. 2006) to lead to a steepening of the $M_{\rm BH}$–σ relation. This slope evolution seen in Illustris also naturally explains the slope steepening found in local massive ellipticals and brightest cluster galaxies. However we caution that the detailed comparison with observations can be systematically biased depending on how stellar velocity dispersion is measured, for example, and that these biases are likely more severe at $z > 0$. For future observations it will be of prime importance to disentangle these effects from a genuine redshift evolution of the scaling relations to understand how AGN feedback operates as a function of cosmic time.

(vii) Comparison of the AGN luminosity function predicted by the Illustris simulations with observations reveals that on average AGN radiative efficiencies need to be low if we are to simultaneously match the black hole mass density, mass function and the normalization of the $M_{\rm BH}$–$M_{\rm bulge}$ and $M_{\rm BH}$–σ relations, unless the bolometric corrections are currently largely underestimated. This result is in line with the conclusions drawn by Ueda et al. (2014) based on the hard X-ray data and is driven by the revised black hole–host galaxy scaling relations (Kormendy & Ho 2013; McConnell & Ma 2013) with respect to the past findings (Yu & Tremaine 2002; Häring & Rix 2004). While we cannot uniquely predict radiative efficiencies as they are degenerate with the black hole feedback efficiencies in our model, on average low $\epsilon_{\rm r}$ values indicate that a larger fraction of AGN luminosity needs to couple efficiently with the surrounding gas. Given that for the Illustris simulation we have adopted $\epsilon_{\rm r} = 0.2$ and $\epsilon_{\rm f} = 0.05$, the inferred low radiative efficiencies imply that the feedback efficiency needs to be a factor 2–4 higher (as the product of the two is degenerate in our model). While such high feedback efficiencies are not ruled out observationally yet, different accretion models than the one assumed in Illustris and/or a possibility of super-Eddington accretion may alleviate the need for very high feedback efficiencies. Future observations of black hole duty cycles and Eddington ratio distributions as a function of redshift and black hole mass will help to shed light on these issues.

(viii) While the shape of the bolometric and hard X–ray luminosity functions is in very good agreement with the data at $z = 0$ and 1, at higher redshifts we overpredict the number of faint AGN. By restricting our sample to black holes more massive than $5 \times 10^7\,{\rm M}_{\odot}$ we can get a much better match to the data, indicating again that our seeding prescription and poorly resolved accretion on to low-mass black holes could be responsible for this discrepancy. We furthermore caution that comparison of volume-limited versus flux-limited samples, bolometric corrections and cosmic evolution of the fraction of Compton-thick sources are additional sources of uncertainty.

(ix) We find that in the Illustris AGN population there is evidence for cosmic downsizing (Barger et al. 2005; Hasinger 2008; Ueda et al. 2014). Not only does the distribution of Eddington ratios evolve with redshift in broad agreement with cosmic downsizing, but we directly show that the simulated number densities of AGN, split into different hard X-ray luminosity bins, exhibit systematically steeper drops with redshift for more luminous objects. We do not find however that the number density of lower luminosity AGN peaks at lower redshifts in Illustris, unless low-mass black holes are excluded from the analysis.

(x) We finally explore the physical link between star formation and black hole accretion triggering. Current observations have struggled to find clear evidence of such a link (e.g. see Alexander & Hickox 2012; Azadi et al. 2015; Hickox et al. 2014, and the references therein), thus questioning the standard lore where due to mergers galaxies and black holes grow hand-in-hand. We find that the black hole X-ray luminosities (direct proxies of the accretion rates) are correlated with the host galaxy star formation rate – in accordance with the similar shapes of the cosmic star formation and black hole accretion rate density – albeit with a large scatter. Current observations probe a too narrow dynamic range in X-ray luminosities to see this correlation, even though it can be inferred if the spectroscopically confirmed COSMOS data (Brusa et al. 2010; Lusso et al. 2010, 2011; Bongiorno et al. 2012) at all redshifts are combined together. Large scatter seen in the simulated SFR–$L_{2-10\,{\rm keV}}$ relation demonstrates that the physical link between star formation and black hole accretion triggering is more complex than previously envisaged. Gas-rich major mergers are responsible for the starburst–AGN connection but relative timing offsets (see also Wild, Heckman & Charlot 2010), whereby luminous quasars light-up with a delay, contribute to the scatter. Moreover, in the case of large-scale gas inflows and minor mergers star formation events might not be followed by black hole accretion because of gas consumption, expulsion or a residual angular momentum barrier. Finally, the much shorter time-scale of AGN variability with respect to star formation can also introduce scatter as, for example, discussed in a recent paper by Hickox et al. (2014), which is in line with our findings.

Large-scale cosmological simulations such as Illustris where thousands of galaxies are sufficiently well resolved to study their morphological properties are a unique tool to dissect the cosmological co-evolution (or the lack thereof) for representative samples of galaxies and their central black holes in the Universe. In fact, the results of our black hole model presented in this work should be viewed in a wider context of reproducing a number of key features of a representative sample of galaxies (Genel et al. 2014a; Vogelsberger et al. 2014a), and specifically in quenching and morphologically transforming massive galaxies thanks to the AGN feedback. Studying black hole growth and feedback with future improved simulations will be more timely than ever and promises to give us an ever more precise understanding of the astrophysical role these fascinating objects play.

ACKNOWLEDGEMENTS

We would like to thank the referee for a very constructive referee report which improved this paper. DS would like to thank Martin Haehnelt, Manda Banerji, Roberto Maiolino, Matt Auger, Ranjan Vasudevan, Andy Fabian and Richard McMahon for very useful discussions. DS also would like to thank Manda Banerji for kindly providing the data compilation used in Fig. 13. Simulations were run on the Harvard Odyssey and CfA/ITC clusters, the Ranger and Stampede supercomputers at the Texas Advanced Computing Center as part of XSEDE, the Kraken supercomputer at Oak Ridge National Laboratory as part of XSEDE, the CURIE supercomputer at CEA/France as part of PRACE project RA0844 and the SuperMUC computer at the Leibniz Computing Centre, Germany, as part of project pr85je. VS acknowledges support by the DFG Research Centre SFB-881 'The Milky Way System' through project A1, and by the European Research Council under ERC-StG EXAGAL-308037. SG acknowledges support provided by NASA through Hubble Fellowship grant HST-HF2-51341.001-A awarded by the STScI, which is operated by the Association of Universities for Research in Astronomy, Inc., for NASA, under contract NAS5-26555. GFS acknowledges support from the *HST* grants program, numbers HST-AR- 12856.01-A and HST-AR-13887.004A. Support for programs #12856 and #13887 was provided by NASA through a grant from the Space Telescope Science Institute, which is operated by the Association of Universities for Research in Astronomy, Inc., under NASA contract NAS 5-26555. LH acknowledges support from NASA grant NNX12AC67G and NSF grant AST-1312095.

REFERENCES

Aird J., Coil A. L., Georgakakis A., Nandra K., Barro G., Perez-Gonzalez P. G., 2015, MNRAS, in press (arXiv:1503.01120)
Alexander D. M., Hickox R. C., 2012, New Astron. Rev., 56, 93
Aumer M., White S. D. M., Naab T., Scannapieco C., 2013, MNRAS, 434, 3142
Azadi M. et al., 2015, ApJ, 806, 187
Barger A. J., Cowie L. L., Mushotzky R. F., Yang Y., Wang W.-H., Steffen A. T., Capak P., 2005, AJ, 129, 578
Bauer A., Springel V., 2012, MNRAS, 423, 423, 3102
Bellovary J., Holley-Bockelmann K., Gültekin K., Christensen C., Governato F., Brooks A., Loebman S., Munshi F., 2014, MNRAS, 445, 2667

Birnboim Y., Dekel A., 2003, MNRAS, 345, 349
Bongiorno A. et al., 2012, MNRAS, 427, 3103
Bongiorno A. et al., 2014, MNRAS, 443, 2077
Booth C. M., Schaye J., 2009, MNRAS, 398, 53
Boylan-Kolchin M., Ma C.-P., Quataert E., 2006, MNRAS, 369, 1081
Brusa M. et al., 2010, ApJ, 716, 348
Buchner J. et al., 2015, ApJ, 802, 89
Chabrier G., 2003, PASP, 115, 763
Cicone C., Feruglio C., Maiolino R., Fiore F., Piconcelli E., Menci N., Aussel H., Sturm E., 2012, A&A, 543, A99
Cicone C. et al., 2014, A&A, 562, A21
Ciotti L., Ostriker J. P., Proga D., 2009, ApJ, 699, 89
Costa T., Sijacki D., Trenti M., Haehnelt M. G., 2014a, MNRAS, 439, 2146
Costa T., Sijacki D., Haehnelt M. G., 2014b, MNRAS, 444, 2355
De Rosa G., Decarli R., Walter F., Fan X., Jiang L., Kurk J., Pasquali A., Rix H. W., 2011, ApJ, 739, 56
Di Matteo T., Springel V., Hernquist L., 2005, Nature, 433, 604
Di Matteo T., Colberg J., Springel V., Hernquist L., Sijacki D., 2008, ApJ, 676, 33
Dubois Y., Devriendt J., Slyz A., Teyssier R., 2012, MNRAS, 420, 2662
Fabian A. C., Iwasawa K., 1999, MNRAS, 303, L34
Fan X. et al., 2006, AJ, 131, 1203
Faucher-Giguère C.-A., Lidz A., Zaldarriaga M., Hernquist L., 2009, ApJ, 703, 1416
Ferrarese L., Merritt D., 2000, ApJ, 539, L9
Gebhardt K., Adams J., Richstone D., Lauer T. R., Faber S. M., Gültekin K., Murphy J., Tremaine S., 2011, ApJ, 729, 119
Genel S., Vogelsberger M., Nelson D., Sijacki D., Springel V., Hernquist L., 2013, MNRAS, 435, 1426
Genel S. et al., 2014a, MNRAS, 445, 175
Genzel R. et al., 2014b, ApJ, 796, 7
Guedes J., Callegari S., Madau P., Mayer L., 2011, ApJ, 742, 76
Gültekin K. et al., 2009, ApJ, 698, 198
Haehnelt M. G., Natarajan P., Rees M. J., 1998, MNRAS, 300, 817
Häring N., Rix H.-W., 2004, ApJ, 604, L89
Harris C. E., Bennert V. N., Auger M. W., Treu T., Woo J.-H., Malkan M. A., 2012, ApJS, 201, 29
Hasinger G., 2008, A&A, 490, 905
Hickox R. C., Mullaney J. R., Alexander D. M., Chen C.-T. J., Civano F. M., Goulding A. D., Hainline K. N., 2014, ApJ, 782, 9
Hinshaw G. et al., 2013, ApJS, 208, 19
Hirschmann M., Khochfar S., Burkert A., Naab T., Genel S., Somerville R. S., 2010, MNRAS, 407, 1016
Hirschmann M., Dolag K., Saro A., Bachmann L., Borgani S., Burkert A., 2014, MNRAS, 442, 2304
Hopkins P. F., Hernquist L., Cox T. J., Di Matteo T., Robertson B., Springel V., 2006, ApJS, 163, 1
Hopkins P. F., Richards G. T., Hernquist L., 2007a, ApJ, 654, 731
Hopkins P. F., Hernquist L., Cox T. J., Robertson B., Krause E., 2007b, ApJ, 669, 45
Hopkins P. F., Kereš D., Oñorbe J., Faucher-Giguère C.-A., Quataert E., Murray N., Bullock J. S., 2014, MNRAS, 445, 581
Jahnke K., Macciò A. V., 2011, ApJ, 734, 92
Kassin S. A. et al., 2007, ApJ, 660, L35
Kereš D., Vogelsberger M., Sijacki D., Springel V., Hernquist L., 2012, MNRAS, 425, 2027
Khandai N., Di Matteo T., Croft R., Wilkins S. M., Feng Y., Tucker E., DeGraf C., Liu M.-S., 2015, MNRAS, 450, 1349
King A., 2003, ApJ, 596, L27
Kormendy J., Ho L. C., 2013, ARA&A, 51, 511
Lauer T. R., Tremaine S., Richstone D., Faber S. M., 2007, ApJ, 670, 249
Lusso E. et al., 2010, A&A, 512, A34
Lusso E. et al., 2011, A&A, 534, A110
Lusso E. et al., 2012, MNRAS, 425, 623
Lutz D. et al., 2008, ApJ, 684, 853
Lynden-Bell D., 1969, Nature, 223, 690
McConnell N. J., Ma C.-P., 2013, ApJ, 764, 184
Magorrian J. et al., 1998, AJ, 115, 2285
Mahadevan R., 1997, ApJ, 477, 585
Maiolino R. et al., 2012, MNRAS, 425, L66
Marconi A., Hunt L. K., 2003, ApJ, 589, L21
Marinacci F., Pakmor R., Springel V., 2014, MNRAS, 437, 1750
Merloni A., 2004, MNRAS, 353, 1035
Merloni A., Heinz S., 2008, MNRAS, 388, 1011
Merloni A. et al., 2010, ApJ, 708, 137
Mortlock D. J. et al., 2011, Nature, 474, 616
Mullaney J. R. et al., 2012, MNRAS, 419, 95
Nelson D., Vogelsberger M., Genel S., Sijacki D., Kereš D., Springel V., Hernquist L., 2013, MNRAS, 429, 3353
Okamoto T., Frenk C. S., Jenkins A., Theuns T., 2010, MNRAS, 406, 208
Oppenheimer B. D., Davé R., 2008, MNRAS, 387, 577
Peng C. Y., 2007, ApJ, 671, 1098
Puchwein E., Springel V., 2013, MNRAS, 428, 2966
Rahmati A., Pawlik A. H., Raicevic M., Schaye J., 2013, MNRAS, 430, 2427
Rees M. J., 1984, ARA&A, 22, 471
Robertson B., Hernquist L., Cox T. J., Di Matteo T., Hopkins P. F., Martini P., Springel V., 2006, ApJ, 641, 90
Rosario D. J. et al., 2012, A&A, 545, A45
Salviander S., Shields G. A., 2013, ApJ, 764, 80
Schawinski K. et al., 2014, MNRAS, 440, 889
Schaye J. et al., 2015, MNRAS, 446, 521
Schulze A., Wisotzki L., 2014, MNRAS, 438, 3422
Shankar F., 2013, Classical Quantum Gravity, 30, 244001
Shen Y., Kelly B. C., 2010, ApJ, 713, 41
Shen Y., Kelly B. C., 2012, ApJ, 746, 169
Shields G. A., Menezes K. L., Massart C. A., Vanden Bout P., 2006, ApJ, 641, 683
Sijacki D., Springel V., di Matteo T., Hernquist L., 2007, MNRAS, 380, 877
Sijacki D., Springel V., Haehnelt M. G., 2009, MNRAS, 400, 100
Sijacki D., Springel V., Haehnelt M. G., 2011, MNRAS, 414, 3656
Sijacki D., Vogelsberger M., Kereš D., Springel V., Hernquist L., 2012, MNRAS, 424, 2999
Silk J., Rees M. J., 1998, A&A, 331, L1
Snyder G. F. et al., 2015, MNRAS, submitted, preprint (arXiv:1502.07747)
Somerville R. S., Hopkins P. F., Cox T. J., Robertson B. E., Hernquist L., 2008, MNRAS, 391, 481
Sommer-Larsen J., Dolgov A., 2001, ApJ, 551, 608
Sparre M. et al., 2015, MNRAS, 447, 3548
Springel V., 2010, MNRAS, 401, 791
Springel V., 2011, in van de Weijgaert R., Vegter G., Ritzerveld J., Icke V., eds, Invited review for the volume 'Tessellations in the Sciences: Virtues, Techniques and Applications of Geometric Tilings'. Springer-Verlag, Berlin, in press (arXiv:1109.2218)
Springel V., Hernquist L., 2003, MNRAS, 339, 289
Springel V., Di Matteo T., Hernquist L., 2005, MNRAS, 361, 776
Stinson G. S., Brook C., Macciò A. V., Wadsley J., Quinn T. R., Couchman H. M. P., 2013, MNRAS, 428, 129
Thacker R. J., MacMackin C., Wurster J., Hobbs A., 2014, MNRAS, 443, 1125
Torrey P., Vogelsberger M., Sijacki D., Springel V., Hernquist L., 2012, MNRAS, 427, 2224
Torrey P., Vogelsberger M., Genel S., Sijacki D., Springel V., Hernquist L., 2014, MNRAS, 438, 1985
Torrey P. et al., 2015, MNRAS, 447, 2753
Tremaine S. et al., 2002, ApJ, 574, 740
Treu T., Malkan M. A., Blandford R. D., 2004, ApJ, 615, L97
Ueda Y., Akiyama M., Hasinger G., Miyaji T., Watson M. G., 2014, ApJ, 786, 104
Vasudevan R. V., Fabian A. C., 2007, MNRAS, 381, 1235
Vasudevan R. V., Fabian A. C., 2009, MNRAS, 392, 1124
Vogelsberger M., Sijacki D., Kereš D., Springel V., Hernquist L., 2012, MNRAS, 425, 3024
Vogelsberger M., Genel S., Sijacki D., Torrey P., Springel V., Hernquist L., 2013, MNRAS, 436, 3031
Vogelsberger M. et al., 2014a, Nature, 509, 177

Vogelsberger M. et al., 2014b, MNRAS, 444, 1518
Volonteri M., 2010, A&AR, 18, 279
White S. D. M., Frenk C. S., 1991, ApJ, 379, 52
Wiersma R. P. C., Schaye J., Theuns T., Dalla Vecchia C., Tornatore L., 2009, MNRAS, 399, 574
Wild V., Heckman T., Charlot S., 2010, MNRAS, 405, 933
Willott C. J. et al., 2010, AJ, 139, 906
Woo J.-H., Treu T., Malkan M. A., Blandford R. D., 2008, ApJ, 681, 925
Yu Q., Tremaine S., 2002, MNRAS, 335, 965

APPENDIX: CONVERGENCE ISSUES

Having discussed convergence properties of the black hole accretion rate and mass density in Section 3.1, here we focus on the convergence of the black hole mass function and $M_{\rm BH}$–$M_{\rm bulge}$ relation which we have presented for the highest resolution Illustris simulation in Sections 3.3 and 3.4.

In Fig. A1 we show the black hole mass function at $z = 0$, split by the Eddington ratios of black holes, as indicated in the legend. For each colour thin to thick lines are for Illustris simulations with three different resolutions: 3×455^3, 3×910^3 and 3×1820^3, respectively. There are two important features to notice. While the convergence rate for the total mass function is not very good (similarly to what we found for the black hole accretion rate density), the uncertainty due to this is smaller than the observational uncertainty as estimated by Shankar (2013). Furthermore, the convergence rate significantly improves for black holes with Eddington ratios $\lambda_{\rm Edd} > 10^{-4}$, in particular at the massive end. This is very encouraging given that black holes with higher $\lambda_{\rm Edd}$ will likely influence their host galaxies more than the very radiatively inefficient accretors and also considering that most of the black hole mass is accreted during the radiatively efficient accretion phase. Note also that the black hole accretion model is more robust (and less dependent on subgrid physics details) for the black holes accreting closer to the Eddington rate.

In Fig. A2 we show the stellar half-mass of all galaxies at $z = 0$ versus their central black hole mass for the low- (left) and intermediate (right)-resolution Illustris simulation. The same plot for the high-resolution simulation is illustrated in Fig. 4. Again here the results are reassuring in terms of numerical convergence. If we apply

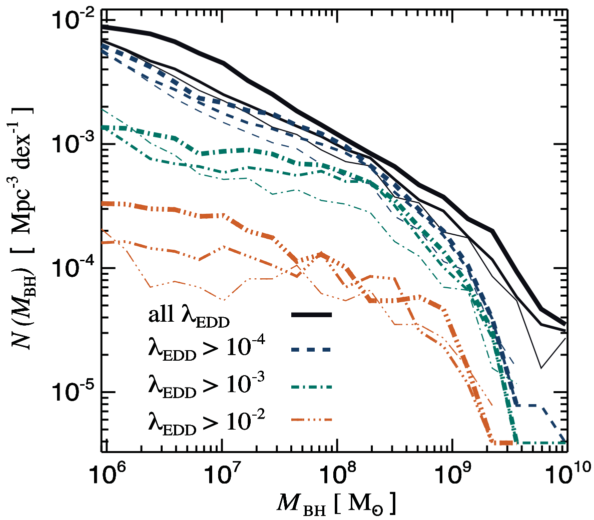

Figure A1. Black hole mass function at $z = 0$, split by the Eddington ratios of black holes, as indicated on the legend. For each colour thin to thick lines are for Illustris simulations with three different resolutions: 3×455^3, 3×910^3 and 3×1820^3, respectively.

the same minimum stellar particle number within the half-mass radius of 80 as we did for our high-resolution run (corresponding to a minimum stellar half-mass of 10^8 M$_\odot$), the best fits yield slopes of 1.61 and 1.37 and normalizations of −9.08 and −6.91 for our low- and intermediate-resolution runs, respectively. Furthermore, from Fig. A2 it is evident that the massive end of the $M_{\rm BH}$–$M_{\rm bulge}$ relation is not significantly affected by resolution effects where for all three runs we reproduce the data well. At the low-mass end the simulated relation shifts somewhat to the right for higher resolutions, which is caused by the combined effect of stellar masses increasing and black hole masses decreasing with higher resolution. We finally note that even the main $g - r$ colour trend along the simulated $M_{\rm BH}$–$M_{\rm bulge}$ relation is present at all resolutions, although with increasing resolution we find a higher fraction of blue star-forming galaxies at the low-mass end.

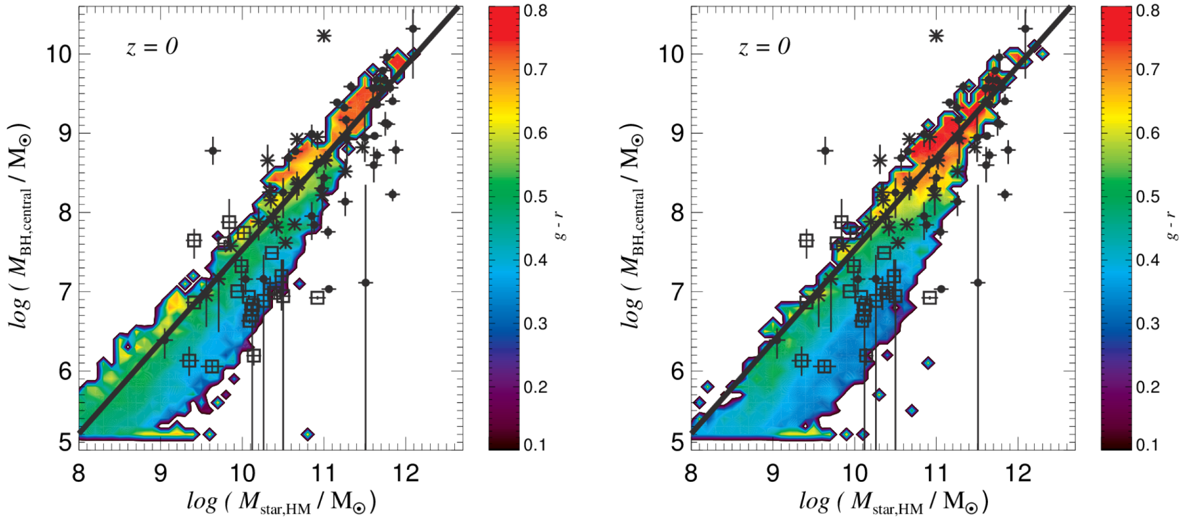

Figure A2. Stellar half-mass of all galaxies at $z = 0$ versus their central black hole mass for the low- (left) and intermediate (right)-resolution Illustris simulation. Colour coding is according to the $g - r$ colours of galaxies. The thick black line denotes the best-fitting $M_{\rm BH}$–$M_{\rm bulge}$ relation from Kormendy & Ho (2013) fitted to ellipticals and galaxies with bulges only. Symbols with error bars are from Kormendy & Ho (2013) as well, where circles are for ellipticals, stars are for spirals with a bulge and squares are for pseudo-bulges.

This paper has been typeset from a TEX/LATEX file prepared by the author.